

AD-782 647

MICROSTRUCTURE STUDIES OF POLY-  
CRYSTALLINE REFRACTORY COMPOUNDS

William H. Rhodes, et al

Avco Corporation

Prepared for:

Naval Air Systems Command

June 1974

DISTRIBUTED BY:

**NTIS**

National Technical Information Service  
U. S. DEPARTMENT OF COMMERCE  
5285 Port Royal Road, Springfield Va. 22151

UNCLASSIFIED

AD-782647

DOCUMENT CONTROL DATA - R & D		
(Security classification of title, body of abstract and indexing annotation must be entered when the overall report is classified)		
1. ORIGINATING ACTIVITY (Corporate author)	2a. REPORT SECURITY CLASSIFICATION	
Avco Corporation Systems Division Lowell, Mass. 01851	Unclassified	
3. REPORT TITLE	2b. GROUP	
Microstructure Studies of Polycrystalline Refractory <del>Compounds</del> <i>Compounds.</i>		
4. DESCRIPTIVE NOTES (Type of report and inclusive dates)		
Summary Report - May 1973 to April 1974		
5. AUTHOR(S) (First name, middle initial, last name)		
William H. Rhodes Rowland M. Cannon, Jr.		
6. REPORT DATE	7a. TOTAL NO. OF PAGES	7b. NO. OF REFS
June 1974	72	21
8a. CONTRACT OR GRANT NO.	8b. ORIGINATOR'S REPORT NUMBER(S)	
N00019-73-C-0376		
9. PROJECT NO.	10. OTHER REPORTS	
	11 (Any other numbers that may be assigned this report)	
10. DISTRIBUTION STATEMENT		
Approved for public release; unlimited distribution		
11. SUPPLEMENTARY NOTES	12. SPONSORING MILITARY ACTIVITY	
	Naval Air Systems Command Washington, D.C.	
13. ABSTRACT		
<p>The program was divided into three tasks within the general topic of microstructure effects on the properties of polycrystalline ceramics. Further modifications were made in the press forging of three-inch <math>Al_2O_3</math> hemispheres to eliminate cracking and surface reactions and yet maintain optical transmission resulting from crystallographic texture and high density. Further forgings of <math>Cr_2Ni</math> were conducted. Process modifications resulted in densities of over 98% with little or no edge cracking. Strengths of forged materials were near those expected for good hot pressed material.</p> <p>Three additional <math>Al_2O_3</math> powders were investigated in the continuing effort to identify and eliminate strength limiting flaws in hot pressed <math>Al_2O_3</math>. An in-house screening treatment was found to remove some of the worst flaws and to increase the average strength. The predominant flaws found were large grain size zones and particulate inclusions. Fractography allowed identification of flaw sizes in some cases. These were typically much larger than the average grain size. Analysis indicated that such flaws can lead to non-zero origins on Petch plots of strength-grain size; this provides an alternative explanation to microplastic fracture initiation in terms of process related large flaws. Fracture surface energies calculated from the indicated flaw size were much closer to those directly measured for single crystals than for polycrystalline material.</p> <p>Measurements of the solubility of carbon in <math>Al_2O_3</math> were made after annealing in CO and <math>CO_2</math>. The results indicated the carbon content from gas solubility to be below 100 ppm at 1600°-1700°C and so less than that often measured in hot pressed</p>		

DD FORM 1473  $Al_2O_3$  bodies.

UNCLASSIFIED

Security Classification

Details of illustrations in  
this document may be better  
studied on microfiche.

UNCLASSIFIED

Security Classification

14. KEY WORDS	LINK A		LINK B		LINK C	
	ROLE	WT	ROLE	WT	ROLE	WT
Hot Pressing Press Forging Mechanical Properties Brittle Fracture Defect Analysis						

UNCLASSIFIED

Security Classification

MICROSTRUCTURE STUDIES OF POLYCRYSTALLINE  
REFRACTORY COMPOUNDS

Summary Report

May 1973 to April 1974

Contract N00019-73-C-0376

Prepared for  
U.S. Naval Air Systems  
Washington, D.C.

Approved by



T. Vasilos

Prepared by

W.H. Rhodes  
R.M. Cannon

AVCO CORPORATION  
Systems Division  
Lowell, Massachusetts 01851

Approved for Public Release: Distribution Unlimited.

FOREWORD

This report was prepared by the Systems Division of Avco Corporation under U.S. Navy Contract N00019-73-0376 entitled, Microstructure Studies of Polycrystalline Compounds.

The work was administered under the direction of the U.S. Department of the Navy, Air Systems Command, with Mr. Charles F. Bersch, Code AIR-52032A, acting as Project Engineer.

This report covers work conducted from May 1973 to April 1974.

The writers are pleased to acknowledge the contributions of the following individuals to this program; B. MacAllister for mechanical evaluation, C.L. Houck for ceramographic preparation, J. Centorino, P. Foley, G. Ross, and E. Vallante for materials preparation, and T. Vasilos for useful discussions. Also Dr. N. Dutta of the U.S. Army Materials and Mechanics Research Center is acknowledged for helpful discussions in the area of flaw analysis.

V

ABSTRACT

The program was divided into three tasks within the general topic of microstructure effects on the properties of polycrystalline ceramics. Further modifications were made in the press forging of three-inch  $Al_2O_3$  hemispheres to eliminate cracking and surface reactions and yet maintain optical transmission resulting from crystallographic texture and high density. Further forgings of  $Si_3N_4$  were conducted. Process modifications resulted in densities of over 98% with little or no edge cracking. Strengths of forged materials were near those expected for good hot pressed material.

Three additional  $Al_2O_3$  powders were investigated in the continuing effort to identify and eliminate strength limiting flaws in hot pressed  $Al_2O_3$ . An in-house screening treatment was found to remove some of the worst flaws and to increase the average strength. The predominant flaws found were large grain size zones and particulate inclusions. Fractography allowed identification of flaw sizes in some cases. These were typically much larger than the average grain size. Analysis indicated that such flaws can lead to non-zero origins on Petch plots of strength-grain size; this provides an alternative explanation to microplastic fracture initiation in terms of process related large flaws. Fracture surface energies calculated from the indicated flaw size were much closer to those directly measured for single crystals than for polycrystalline material.

Measurements of the solubility of carbon in  $Al_2O_3$  were made after annealing in CO and  $CO_2$ . The results indicated the carbon content from gas solubility to be below 100 ppm at  $1600^\circ - 1700^\circ C$  and so less than that often measured in hot pressed  $Al_2O_3$  bodies.

TABLE OF CONTENTS

I. INTRODUCTION . . . . .	1
II. FLAWS IN ALUMINA AND THEIR EFFECT ON STRENGTH . . . . .	2
A. General . . . . .	1
B. Powder Characterization . . . . .	3
C. Consolidation . . . . .	9
D. Transverse Bend Strength and Flaw Analysis . . . . .	20
E. Discussion . . . . .	30
F. Conclusions . . . . .	41
III. PRESS FORGING . . . . .	41
A. General . . . . .	41
B. Raw Materials and Preforms . . . . .	42
C. Press Forging Procedure . . . . .	43
D. Textural Analysis . . . . .	44
E. $Al_2O_3$ Hemisphere Forging Results . . . . .	44
F. $Si_3N_4$ Forging Results . . . . .	46
G. Conclusions . . . . .	46
IV. VOLATILE SPECIES IN HOT PRESSED $Al_2O_3$ . . . . .	57
A. General . . . . .	57
B. Experimental . . . . .	58
C. Results . . . . .	58
D. Conclusions . . . . .	60
V. REFERENCES . . . . .	61

LIST OF TABLES

Table I	Properties of Alumina Powders . . . . .	3
Table II	Results of 3 gm Particulate Impurity Survey . . . . .	9
Table III	Fabrication Conditions and Results . . . . .	11
Table IV	Fracture Strength and Flaw Analysis . . . . .	24
Table V	Summary of Flaw Analysis . . . . .	27
Table VI	Calculated and Measured Fracture Surface Energies . .	40
Table VII	Hemispherical $\text{Al}_2\text{O}_3$ Forging Experiments . . . . .	46
Table VIII	$\text{Si}_3\text{N}_4$ Forgings . . . . .	50
Table IX	Mechanical Properties of Forged $\text{Si}_3\text{N}_4$ . . . . .	56
Table X	Apparent Carbon Solubility in $\text{Al}_2\text{O}_3$ . . . . .	59



## LIST OF ILLUSTRATIONS

Figure 1	Vendor IV $Al_2O_3$ Powder Morphology Showing (a) agglomerate morphology, (b) crystallite morphology, and (c) porosity within some crystallites . . . . .	4
Figure 2	Vendor V $Al_2O_3$ Powder Showing (a) agglomerate morphology, (b) crystallite morphology, and (c) crystallites approaching 200 Å in diameter . . . . .	5
Figure 3	Vendor VI Powder Showing (a) agglomerate structure, and (b) crystallite morphology . . . . .	6
Figure 4	Alum Derived Vendor II Powder Showing (a) agglomerate structure, and (b) crystallite morphology . . . . .	7
Figure 5	Particulate Impurities Found in (a) Vendor II powder after treatment, and (b) as-received Vendor VI powder (substitute lot) . . . . .	10
Figure 6	Microstructure of Vendor II Billet 1007 With a Grain Size of 2.0 $\mu m$ . . . . .	13
Figure 7	Unidentified Flaws in Billet 1007 . . . . .	14
Figure 8	Microstructure of Billet D1940 Pressed with Vendor IV Powder . . . . .	15
Figure 9	Defects in Billet D1940 Judged to be (a) lens shaped pore zone resulting from reaction, and (b) large void and pore ring also resulting from a reaction . . . . .	16
Figure 10	Microstructure of Billet D1907 Pressed with Vendor V Powder . . . . .	17
Figure 11	Second Phase Inclusions Found in Billet D1907 . . . . .	18
Figure 12	Microprobe Analysis of Inclusion in Vendor V Billet D1907 Showing Presence of Cu and Zn in Addition to the Matrix Al . . . . .	19
Figure 13	Microstructure of Billet 1417 Fabricated with Vendor VI Powder and Having 1.25 $\mu m$ Grain Size . . . . .	21
Figure 14	Defects in Billet 1417 from Vendor VI Powder Showing (a) high porosity pocket, and (b) an inclusion . . . . .	22
Figure 15	specimen 1007-5 Showing (a) center origin, (b) medium magnification view showing unusual rod-like grain structure, and (c) high magnification view of fracture origin . . . . .	26

LIST OF ILLUSTRATIONS continued

Figure 16	Specimen 1940-5 Showing Lenticular Pore at Fracture Origin . . . . .	29
Figure 17	Specimen 1907-5 Showing (a) fracture origin near center of bar, (b) subsurface pit and particle, and (c) higher magnification view of defect . . . . .	31
Figure 18	Microprobe study of fracture origin in Specimen 1907-5 showing (a) secondary emission of area around defect shown in Figure 17; (b) Cu emission; (c) Al emission; (d) backscattering from defect area; (e) Fe emission; and (f) accumulative X-ray emission(sample coated with Au and Pd) . . . . .	32
Figure 19	Specimen 1331-1 Showing (a) entire fracture surface, (b) subsurface defect as fracture origin, and (c) defect structure to include faceted pore and exaggerated grain growth . . . . .	33
Figure 20	Fracture Surface of 1326-2, 61.7 Kpsi Specimen Showing (a) fracture origin, and (b) transgranular fracture at fracture origin . . . . .	34
Figure 21	Room Temperature Bend Strength versus Grain Size or Flaw Size ( $\frac{1}{2}$ flaw size for internal flaws) Compared with Literature Strength-Grain Size Data . . . . .	36
Figure 22	Room Temperature Bend Strength versus Square Root of Inverse Flaw Size ( $\frac{1}{2}$ flaw size for internal flaws) . . . . .	38
Figure 23	Forging 1986 from a presintered preform illustrating elimination of rim and apex cracks and reaction . . . . .	47
Figure 24	Microstructure of vacuum annealed piece of hemisphere 1838 showing coarse, partially spherodized porosity and two distinct regions with different porosity levels. . . . .	49
Figure 25	Rim Section of Forged $\text{Si}_3\text{N}_4$ , Billet D1905 Showing Moderate Porosity and Interpenetration of BN or Related Phase . . . . .	51
Figure 26	Central Section of Forged $\text{Si}_3\text{N}_4$ , Billet D1905 Showing High Density and Iron Silicide Phase . . . . .	52
Figure 27	As-polished microstructure of forged $\text{Si}_3\text{N}_4$ , 1972, showing regions of high porosity . . . . .	53
Figure 28	Inverse Pole Figure for Forged Silicon Nitride . . . . .	55

## I. INTRODUCTION

This program has been concerned with the effect of fabrication and microstructural and chemical variables on physico-mechanical properties of ceramics. Three areas have been studied separately, although there are important interrelations between the areas. Studies to identify the origin of flaws and the effect of such flaws on the strength of hot pressed  $\text{Al}_2\text{O}_3$  have continued with investigation of three additional  $\text{Al}_2\text{O}_3$  powders and billets made from them. In-house processing techniques were used to reduce flaws and so to increase the strength of  $\text{Al}_2\text{O}_3$ . Mechanical strength tests and fractography have been correlated with analysis of the powder in this effort. Studies on hot forging of both  $\text{Al}_2\text{O}_3$  and  $\text{Si}_3\text{N}_4$  have also been continued. Processing modifications to eliminate cracking and reaction during forging of  $\text{Al}_2\text{O}_3$  hemispheres were investigated. Forging of  $\text{Si}_3\text{N}_4$ , indicated previously to be feasible, was further investigated to determine the proper forging conditions; strengths were also measured to indicate the effects of forging. Finally, the considerations of the effects of gaseous impurities on hot pressed  $\text{Al}_2\text{O}_3$  started last year were extended with measurements of the solubility of carbon in  $\text{Al}_2\text{O}_3$  after controlled annealing in CO and  $\text{CO}_2$ .

## II. FLAWS IN ALUMINA AND THEIR EFFECT ON STRENGTH

### A. General

A number of years ago Pears and Starrett<sup>1</sup> examined the applicability of the Weibull statistical strength analysis to hot pressed  $\text{Al}_2\text{O}_3$  produced by this laboratory. In general, the strength decreased with increased specimen volume in the general way expected by a statistical distribution of flaws and flaw sizes, but no single set of Weibull constants was found. Many of the specimens contained microscopic flaws from 1 to 50 grain diameters, while others appeared generally free of flaws larger than the average grain size. An attempt was made to segregate specimens with obvious flaws, but this did not prove completely successful judging from the inability to find a single set of Weibull constants. In the last two years this program has considered carefully the source and effect of flaws in hot pressed  $\text{Al}_2\text{O}_3$ .<sup>2f,8</sup> It has been found that the three powder sources normally employed in producing hot pressed  $\text{Al}_2\text{O}_3$  all contain particulate impurities which contributed to flaws found randomly in polished structures and predominantly at fracture origins in tested specimens. Undoubtedly some of the observed flaws were introduced by processing errors, although it was not possible to establish the relative distribution of the two sources of flaws. Nearly 70% of the tested specimens contained a readily observed flaw at the fracture origin. Obviously such results have a direct bearing on the work of Pears and Starrett. Further, these results suggest that many previous attempts to relate strength and "average" microstructure suffer from a high incidence of flaw initiated fractures where the flaw size is significantly larger than the grain or pore size.

The present effort considered three new non-sulfate derived powders to determine if another powder process was inherently cleaner, and what effects this would have on strength properties. Further, one of the standard grades of hot pressing powder was treated to remove a large fraction of the particulate impurities, and the effect of this step on strength was measured.

## B. Powder Characterization

Previous reports<sup>2</sup> dealt with characterization of three alum derived powders identified as "Vendors I, II, and III." A lot of treated Vendor II powder was included in the present study, thus the powder characteristics will be repeated. The new powder lots will have designations commencing with Vendor IV. The salient properties of the powders are listed in Table I.

Powder morphology was examined by electron microscopy techniques. Figure 1 illustrates typical characteristics for Vendor IV powder. The powder is considered to be moderately agglomerated. Figure 1b illustrates a typical range of crystallite sizes from 0.1 to 1  $\mu\text{m}$  with an average of about 0.4  $\mu\text{m}$ . Porosity within crystallites is shown in Figure 1b and in greater detail in Figure 1c. The cause of this 500 Å porosity is open to speculation, but the effect is certainly undesirable if they are not annihilated before significant grain growth occurs. This latter condition would, of course, result in pore entrapment within grains and an inability to reach high density.

Figure 2 illustrates the morphology of Vendor V powder. A high degree of agglomeration is observed together with four distinct crystallite morphologies; cubes, rods, spheres, and fine, nearly spherical crystallites with considerable neck growth. This suggests a very unusual path for formation and growth, certainly not the normal nucleation and growth process where a log normal distribution of crystallite size is expected. X-ray analysis of this powder identified delta and possibly theta in addition to the expected alpha  $\text{Al}_2\text{O}_3$ . Some of the finer crystallite morphologies may be associated with the transitional  $\text{Al}_2\text{O}_3$  phases.

Figure 3 shows the results of the powder analysis of Vendor VI powder. The crystallite size distribution and identification has been thoroughly investigated.<sup>2b</sup> Briefly, it was found by a combination of selected area electron diffraction, quantitative analysis of electron micrographs, and quantitative X-ray diffraction that the fine crystallites representing 42 w/o of the sample were transitional  $\text{Al}_2\text{O}_3$  phases and had a mean crystallite size of 240 Å. The remaining phase was  $\alpha\text{-Al}_2\text{O}_3$  with a mean crystallite size of 1500 Å. Within each phase the size distribution was log normal. The discontinuity in particle sizes between the phases suggested that the phase transition was accompanied by accelerated growth kinetics.

The powder morphology of alum derived  $\text{Al}_2\text{O}_3$  has been reported extensively,<sup>2</sup> but it is shown in Figure 4 for comparative purposes. The small crystallites are transitional  $\text{Al}_2\text{O}_3$  phase, whereas the larger crystallites are  $\alpha\text{-Al}_2\text{O}_3$ . Considerable neck formation is evident for the  $\alpha\text{-Al}_2\text{O}_3$  particles, and the morphology is very similar to the Vendor VI powder. These were the only two powders of all the  $\text{Al}_2\text{O}_3$  powders examined which exhibited similar morphology for different precursors. This observation was not pursued further, but certainly warrants a detailed investigation.

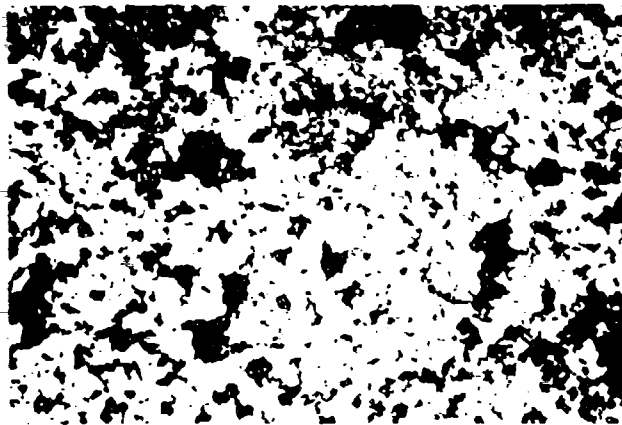
Several of the alum derived powders were subjected to a detailed quantitative particulate impurity analysis.<sup>2f,8</sup> The first technique consisted of surveying 3 gms of powder from a previously unopened container under

TABLE I  
Properties of Alumina Powders

<u>Vendor</u>	<u>Precursor</u>	<u>Particle Size, <math>\mu\text{m}</math></u>	<u>Purity, %</u>	<u>Level* of Major Impurities ppm</u>
II-T	$\text{NH}_4\text{Al}(\text{SO}_4)_2 \cdot 12 \text{H}_2\text{O}$	0.3	$\geq 99.99$	25 $\text{TiO}_2$ , 10 $\text{Fe}_2\text{O}_3$ , 5 $\text{Ca}_2\text{O}_3$
IV	$\text{Al}(\text{OH})_3$	0.4	$\geq 99.93$	60 $\text{Na}_2\text{O}$ , 90 $\text{Fe}_2\text{O}_3$ , 150 $\text{SiO}_2$ , 50 $\text{CaO}$
V	Al	0.5	$\geq 99.99$	20 $\text{SiO}_2$ , 50 $\text{Fe}_2\text{O}_3$
VI	$\text{Al}(\text{NO}_3)_3$	0.2	$\geq 99.995^+$	10 $\text{Na}_2\text{O}$ , 15 $\text{SiO}_2$ , 5 $\text{K}_2\text{O}^+$ , 10 $\text{CaO}$

\*Emission spectroscopy.

+Mass spectrographic analysis.



73042

(a)

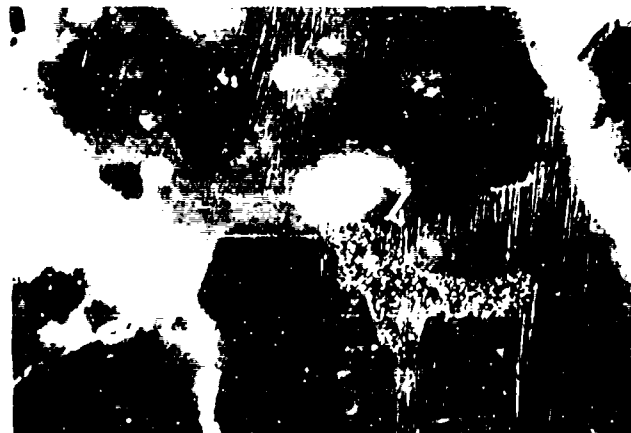
15,00X



73043

(b)

60,000X

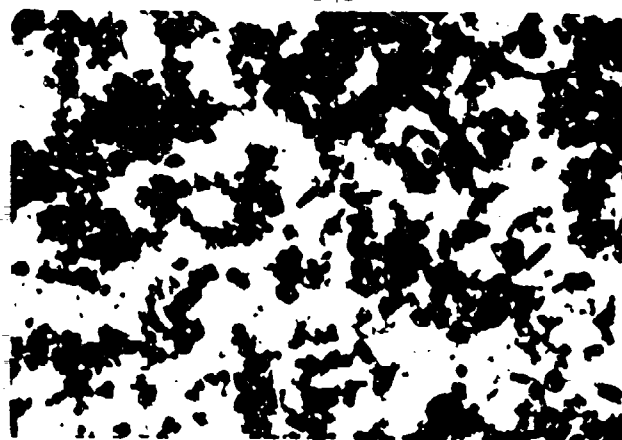


73044

(c)

150,000X

Figure 1. Vendor IV Al<sub>2</sub>O<sub>3</sub> based Magnesia Oxide, (a) agglomerate morphology, (b) crystallite morphology, and (c) porosity within some crystallites.



73130

(a)

1500X



73132

(b)

15,000X



73134

(c)

60,000X

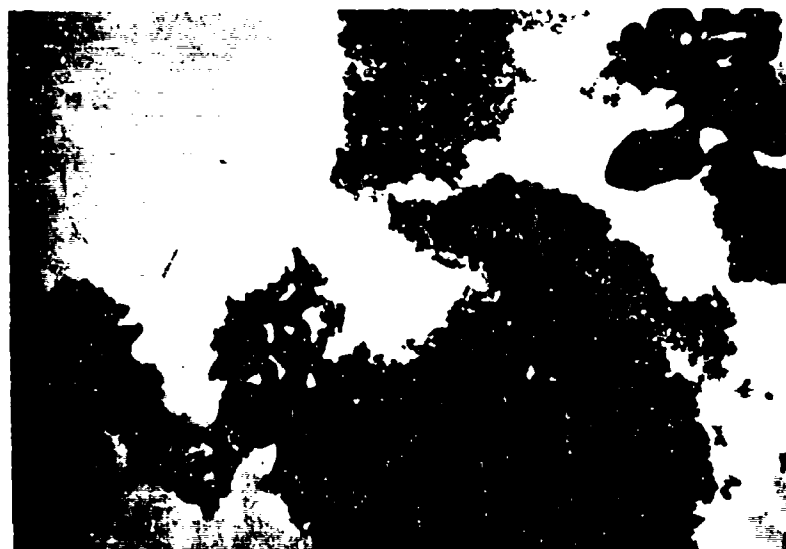
Figure 2. Vendor 7 Al<sub>60</sub> powder showing (a) agglomerate morphology, (b) crystallite morphology, and (c) crystallites approaching 200 Å in diameter.



73038

(a)

1500X



68301

(b)

30,000X

Figure 3. Vendor VI Powder Showing (a) agglomerate structure, and (b) crystallite morphology.



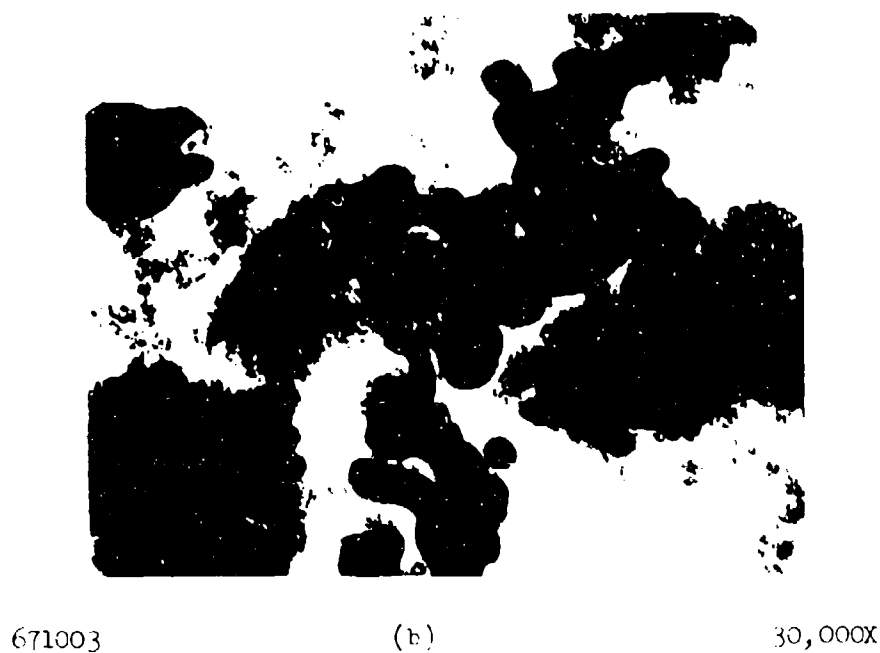
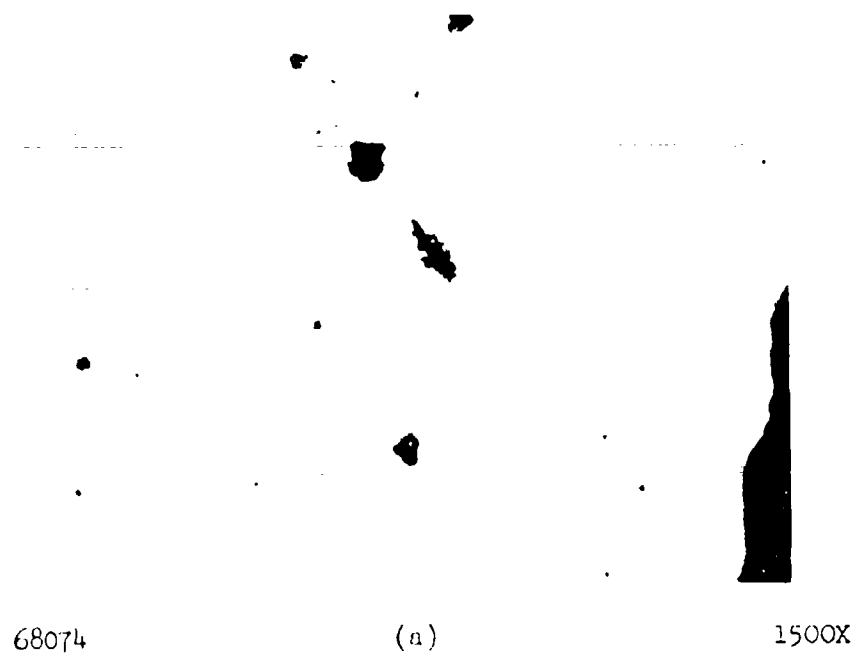


Figure 4. Alum Derived Vendor II Powder Showing (a) agglomerate structure, and (b) crystallite morphology.

an optical stereomicroscope at 10 to 45 X. In the original lot of Vendor II powder, 28 non-alumina particulate impurities were found which translates to 37 particles/cm<sup>3</sup> or one every 0.3 cm in a high density consolidated structure. The second technique consisted of preparing a slurry in a shallow dish, drying, and examining a 2 by 2 inch square area with the dish upside down using bottom lighting. After accounting for the density and depth of focus, analysis of Vendor II powder gave 294 particles/cm<sup>3</sup> or one every 0.15 cm. Thus, it can be seen that the two techniques gave results that differed by about a factor of ten in number per cm<sup>3</sup>, but only a factor of two in spacing. The first technique undoubtedly underestimates the impurity concentration as particles can be overlooked or camouflaged in a survey, and it is concluded that the more tedious slurry technique is more accurate. The current program, however, employed mainly the first or survey technique. The results are given in Table II. The Vendor II results are quoted from the previous results.<sup>28</sup> The treatment of this powder was apparently successful in removing all but the fiber impurities (Figure 5a). Only one 5-20  $\mu$ m black particulate along with one organic appearing fiber was found in Vendor IV powder. No impurities were found in a survey of Vendor V powder. The specific lot of powder employed in making samples for this current effort was exhausted in sample fabrication, so another lot of the same grade was surveyed for foreign particulate impurities to gain a level of incidence experience with the manufacturing process. Vendor VI powder contained black particulates which had a carbon-like appearance (Figure 5b). Although this again is a substitute powder lot, the analysis is thought to be applicable to the actual lot used to fabricate Vendor VI samples as earlier work<sup>2d</sup> had identified 800 ppm C by a fusion technique.

### C. Consolidation

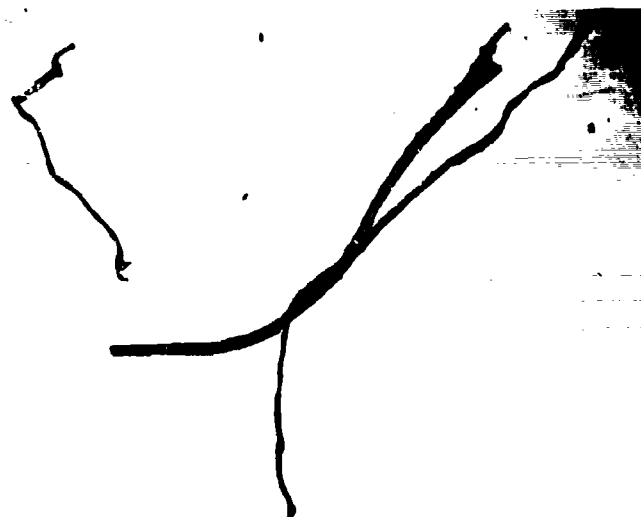
Vendor II, IV, and V powders were consolidated by standard ambient atmosphere pressing techniques while the Vendor VI powder was pressed in a significantly higher pressure regime in vacuum. In addition, the Vendor VI powder had no grain growth additive. The pressing conditions and results are listed in Table III. Additives were introduced by wet milling in a high purity Al<sub>2</sub>O<sub>3</sub> mill for 16 hours. After drying, the powder was sieved through either brass or a nylon screen. Slightly different conditions were employed for the three ambient pressings, but all three powders were judged to be very active and quite suitable for hot pressing. Undoubtedly the hot pressing conditions could be optimized with further consolidation experiments. The grain sizes and relative ranking are consistent with the thermal cycles employed and certainly within the range of expected sizes for hot pressed Al<sub>2</sub>O<sub>3</sub>.

The handling of Vendor VI powder was minimized by eliminating the normal grain growth controlling addition. Also, glove box procedures were employed in the die loading to minimize the chance of contamination. The pressing cycle was worked out after many trials to maximize density and minimize grain size. The use of high strength POCO dies makes this possible without employing grain growth inhibitors. Unlike most other pressed Al<sub>2</sub>O<sub>3</sub>, the product was white and translucent. Pressing 1417 represents near optimum consolidation conditions with a grain size of 1.25  $\mu$ m. The three remaining pressings with this powder (1326, 1331, and 1337) were given a 50 minute longer thermal cycle which resulted in grain growth to 4.8  $\mu$ m. Tests with

TABLE II

Results of 3 gm Particulate Impurity Survey

	<u>Black Particulate</u>	<u>Colorless Particulate</u>	<u>Fiber</u>	<u>Total</u>	<u>Number/ cm<sup>2</sup></u>	<u>Spacing cm</u>
Vendor II	25	1	2	28	37	0.3
Vendor II-T (treated)	0	0	4	4	5.3	0.57
Vendor IV	1	0	1	2	2.6	0.73
Vendor V	0	0	0	0	0	-
Vendor VI	5	0	0	5	6.6	0.53



5871-4

(a)

50X



5871-3

(b)

100X

Figure 5. Particulate Impurities Found in (a) Vender II powder after treatment, and (b) as-received Vender VI powder (substitute lot).

TABLE III  
Fabrication Conditions and Results

<u>Billet Designation</u>	<u>Powder</u>	<u>Additive</u>	<u>Temp. °C</u>	<u>Pressure psi</u>	<u>Time min.</u>	<u>Density gm/cm<sup>3</sup></u>	<u>Grain Size, <math>\mu</math>m *</u>
1007	Vendor II	0.2 MgO 0.1 NiO	1440	5700	125	3.977	2.0
D1940	Vendor IV	0.2 w/o MgO	1440	5000	115	3.953	2.5
D1907	Vendor V	0.15 w/o MgO	1520	4000	90	3.931	3.6
1417	Vendor VI	None	1400	15,000	10	3.971	1.25
1326	Vendor VI	None	1400	15,000	60	-	4.8
1331	Vendor VI	None	1380	15,000	67	3.989	~ 4.8
1337	Vendor VI	None	1400	15,000	60	3.990	~ 4.8

\*Linear intercept corrected by 1.5.

these samples were separated into two groups according to grain size.

The microstructure of Billet 1007 fabricated with treated Vendor II powder is illustrated in Figure 6. Little or no porosity was observed on the as-polished surface. As illustrated in Figure 6b, an equiaxed grain structure was observed. Figure 7 illustrates the only flaws found in the microstructural examination. These have not been identified, but could be either second phase inclusions or high porosity pockets.

The microstructure of Billet D1940 fabricated with the Vendor IV powder is illustrated in Figure 8. A number of polishing scratches are apparent in Figure 8a, but basically a dense  $Al_2O_3$  structure was observed. Small high reflectivity second phase particles are also apparent in this micrograph. The sample was slightly over-etched, but it is possible to state that a very fine equiaxed grain structure was achieved. Attention has been called to the second phase particles in Figure 8. Potentially more serious defects are illustrated in Figure 9. The defect in Figure 9a is 1000  $\mu m$  long and that in Figure 9b is 500  $\mu m$  long. Also, there is the possibility that they have not been sectioned at their midpoint, so the critical dimension may be even longer. The defect in Figure 9a appears to include some second phase interaction phases suggesting an inorganic origin. It is possible, however, that the defect resulted from an organic fiber which carbonized and reacted during hot pressing. The defect in Figure 9b is a lenticular shaped void with a partial ring of pores. The structure was thought to arise from volatilization of some impurity species. There is no evidence for chemical interactions resulting in second phases which suggests that the impurity could be organic in nature.

The microstructure of Billet D1907 fabricated with the Vendor V powder is illustrated in Figure 10. The high density of the structure is confirmed in Figure 10a. The grain structure illustrated in Figure 10b is equiaxed and apparently free of entrapped porosity. Some tendency for exaggerated grain growth was present, but it was judged to be approximately equivalent to many of the structures observed for billets fabricated from alum derived powder. Figure 10a also illustrates the presence of particulate second phase impurities which are shown at higher magnification in Figure 11. Figure 11a shows a cluster of the second phase particles as well as a dozen or so particles scattered throughout the structure. Figure 11b illustrates a 40  $\mu m$  second phase particle which, based on reflectivity, appears similar to those of Figure 11a. Based on the dark recessed region surrounding the central white spot, the phase appears softer than the matrix  $Al_2O_3$ . Attempts to measure hardness were largely unsuccessful due to the small inclusion size. However, hardness indentations were larger than those in the matrix. This certainly suggests that the inclusions are metallic. A microprobe analysis was conducted on one of these inclusions with the results of accumulative counting shown in Figure 12. Cu and Zn were identified which suggests that this sample was contaminated with brass. Since the powder was screened through a brass screen at one point in the Avco fabrication process, this process step is the most logical source of the observed contamination. This conclusion is supported by the fact that no particulate contamination was found in the Vendor V powder analysis (Table II).



5862-1

(a)

100X



73108

(b)

1500X

Figure 6. Microstructure of Vendor II Billet 1007 With a Grain Size of 2.0  $\mu\text{m}$ .

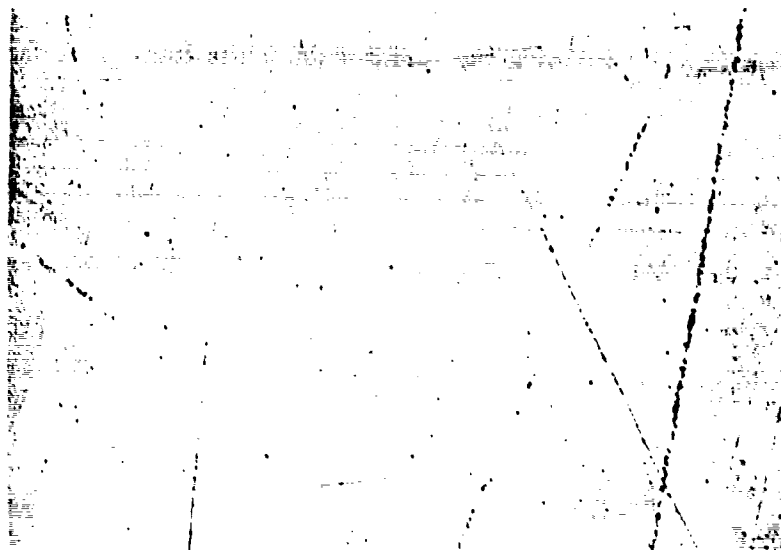


5862-3

1000X

Figure 7. Unidentified Flaws in Billet 1007.

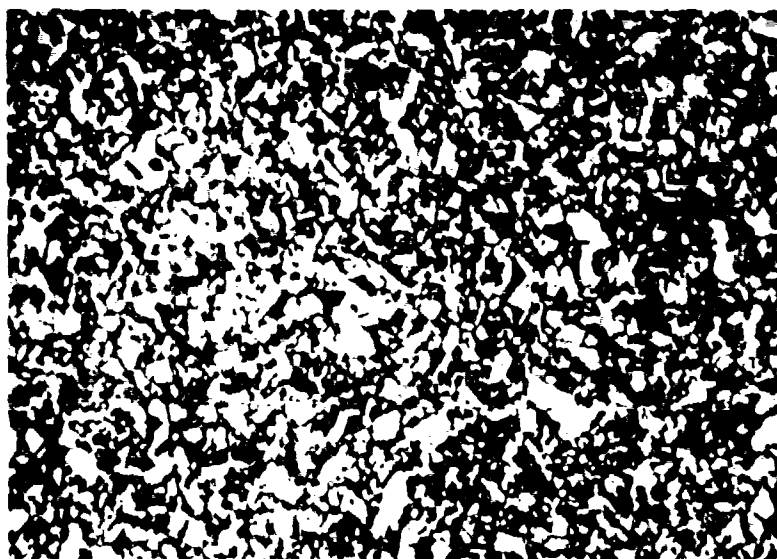




5831-3

(a)

100X

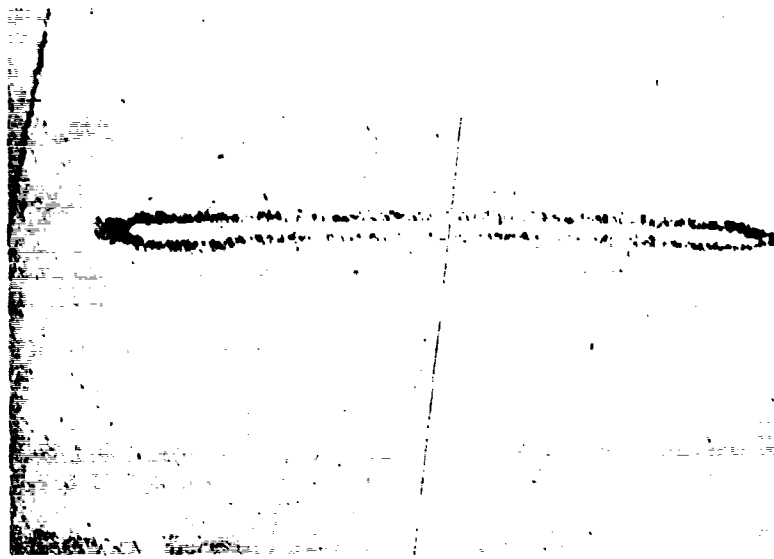


5831-5

(b)

1000X

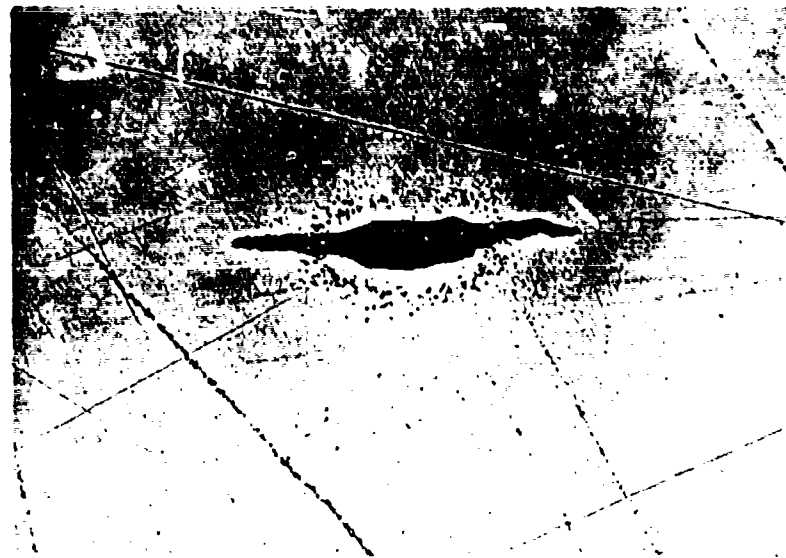
Figure 8. Microstructure of Billet D1970 Pressed with Vendor IV Powder.



5831-1

(a)

10X



5831-2

(b)

10X

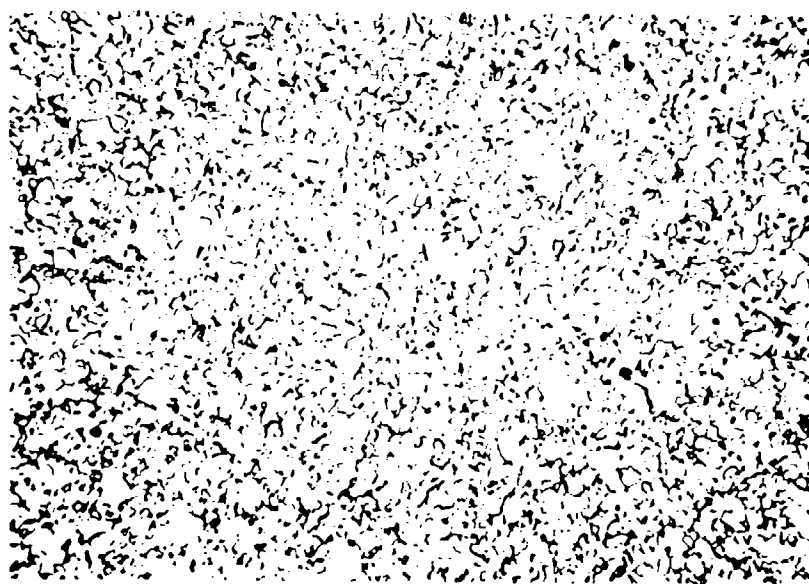
Figure 9. Defect in Pillet 11700 Judged to be (a) large impact pore zone resulting from reaction, and (b) large void and pore ring also resulting from a reaction.



5825-1

(a)

100X

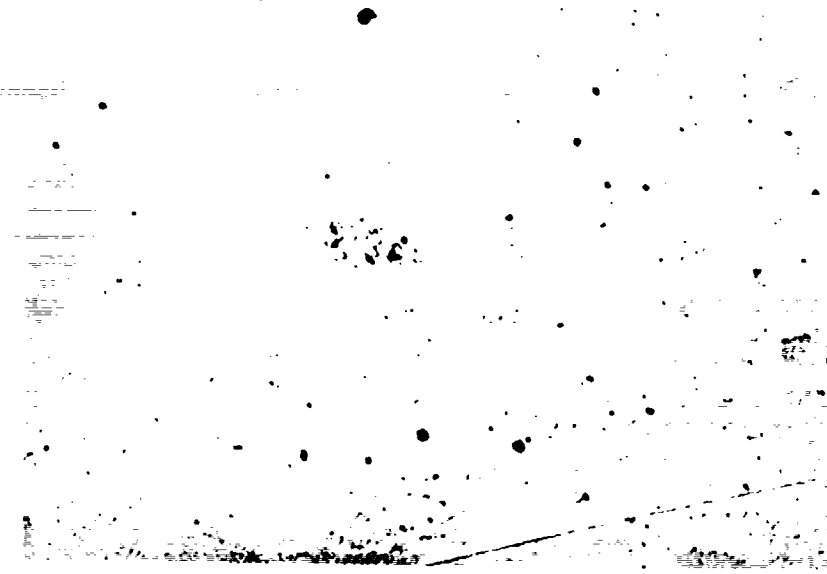


5825-3

(b)

500X

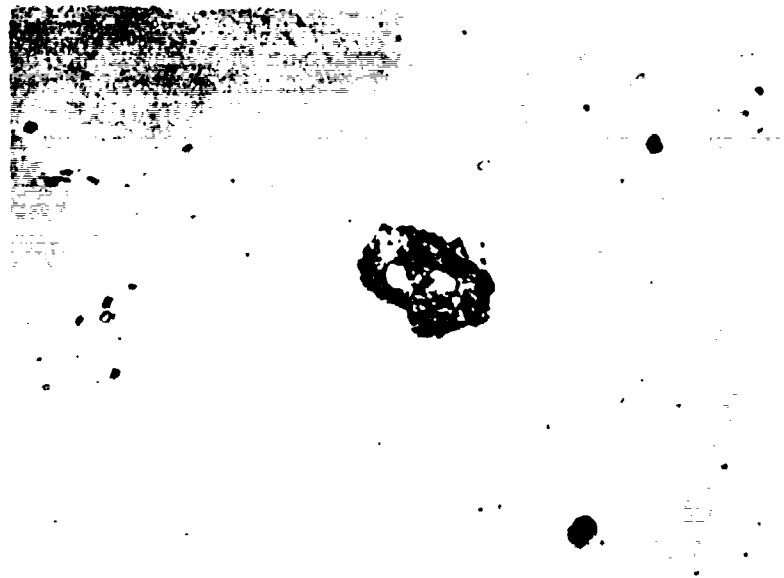
Figure 10. Microstructure of Billet D1907 Pressed with Vendor V Powder.



5825-5

(a)

500X



5825-6

(b)

500X

Figure 11. Second Phase Inclusions Found in Billet D1907.

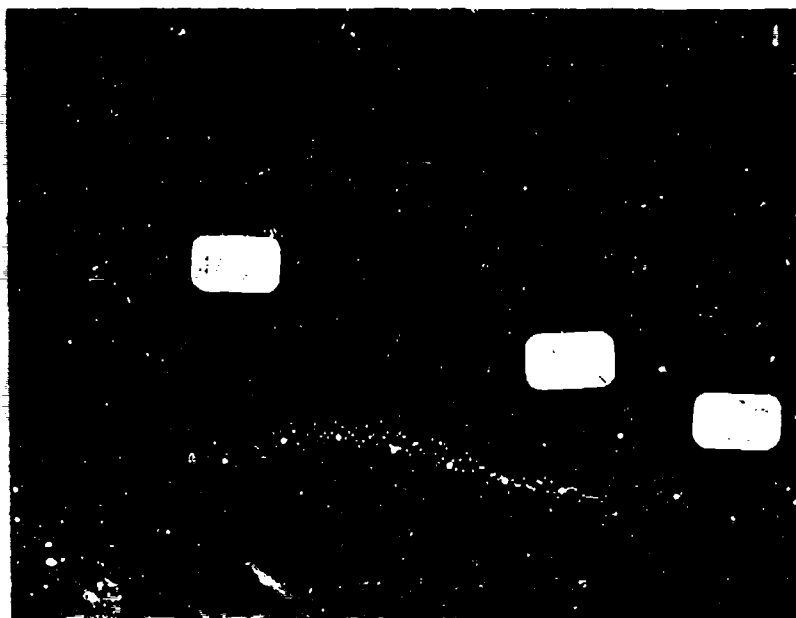


Figure 12. Micrograph of incursion in Vender V Billet 12 of the debris fragments of the in addition to the debris in.

The microstructure of Billet 1417 fabricated with Vendor VI powder is illustrated in Figure 13. The as-polished structure was for the most part dense and uniform (the polishing scratches make this somewhat difficult to discern). The replica of the fractured surface (Figure 13b) reveals a somewhat finer grain size than any of the other billets tested which verified that the absence of grain growth inhibitor can be offset by a reduction in the thermal cycle. Figure 14 illustrates two types of defects found in this billet; a zone of higher than normal porosity, and a 30  $\mu\text{m}$  particulate inclusion. These were typical defects and were repeated in the section examined. The zones of high porosity also are fine grained as the high pore concentration retards grain growth. This high porosity/fine grain size defect is thought to be a pocket where agglomerate bridging has prevented adequate particle contact for solid state diffusion and sintering. There was no evidence that this defect has a chemical origin. Billets 1326, 1331, and 1337, also fabricated from Vendor VI powder, were very similar to the billet illustrated except for the larger grain size.

Also noted in several of the billets (1940, 1326, 1331, 1337, 1417) were defects called spherical shade zones. These defects contained no obvious inclusions as detailed by optical microscopy and were of several shadings relative to the matrix: light color spheres with no distinct boundary, dark color spheres with no distinct boundary, and light spheres with a distinct ring and halo effect. Most often they blend with the matrix when observed at high magnification in reflected light. It is judged that this type of defect arises from process related problems such as the formation of a large agglomerate bridge which fails to break up during ball milling or the addition of the grain growth inhibitor.

Another type of defect (not specifically illustrated by a micrograph) is exaggerated grain growth, and this may be one of the more prominent defects in hot pressed  $\text{Al}_2\text{O}_3$ . Clusters of 20-30  $\mu\text{m}$  grains have been found<sup>28</sup> and grains half this size could still act as defects from a strength viewpoint. Such defects could arise from inadequate mixing of the grain growth inhibitor, impurity promotion of grain growth, inclusion of a large  $\text{Al}_2\text{O}_3$  grain in the powder, or perhaps just the statistical fluctuation of grain growth leading to the discontinuous process.

#### D. Transverse Bend Strength and Flaw Analysis

Strength measurements were conducted in four point bending in ambient air with a relative humidity of  $\sim 55\%$  and in a dry environment. This environment was achieved by heating the bend specimen to  $900^\circ\text{C}$  in vacuum, cooling to room temperature, and backfilling with argon prior to performing the test. The strain rate employed in testing was  $7 \times 10^{-5} \text{ sec}^{-1}$ . The final finish on the specimen surface was obtained with a 400 grit wheel with the grinding direction parallel to the specimen axis.

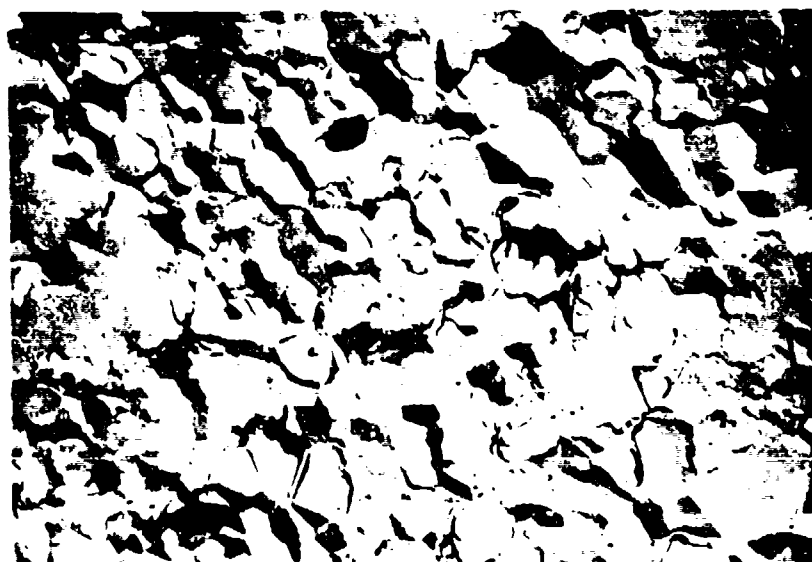
All testing was conducted in a ball bearing and stainless steel test fixture designed to reduce knife edge concentration and frictional effects. Consideration was also given to the shifting of the point of tangency at the load and support points. Vrooman and Ritter<sup>3</sup> have shown this to be a serious problem at high deflections, requiring a numerical analysis to obtain corrected stresses. The error in stress for the fixture



5051-

(a)

100X



691733

(b)

100X

Figure 13. Microstructure of PIPet 141 Radioluted with Tensar VI Powder and Having 1.5  $\mu$ m Grain Size.



5051-1

(a)

100X



5051-1

(b)

100X

Figure 14. 100X micrograph of 100% porous polymer (a) high pore 10% porous, and (b) low pore 10%.



employed was calculated to be 0.025% at 100,000 psi. At this level and with the standard deviations usually found in  $Al_2O_3$  testing, it was considered unnecessary to employ the numerical analysis. Shand<sup>4</sup> has discussed the interpretation of fracture features on glass including the mirror region of smooth crack extension from a flaw, crack branching, and interaction of the crack front with stress waves reflected from nearby surfaces to form wallner lines. Kirchner et al<sup>5</sup> recently demonstrated that these regions may be identified in polycrystalline  $Al_2O_3$  and are useful in some cases to find the fracture origin. Further, fracture origins could be located in several of their bars. Similar techniques were employed in this study.

Bend strengths are reported in Table IV along with the results of a detailed flaw analysis employing a combination of stereo and reflected light microscopy techniques. A number of samples were examined by scanning electron microscopy where defects could not be positively identified by optical microscopy. However, even with this higher magnification examination, uncertainty exists as to the origin of a number of fractures. This is indicated in Table IV. The entire flaw analysis is summarized in Table V. In several cases where uncertainty in the flaw origin existed, an arbitrary selection was made. Billet 1007 exhibited a low percentage of defects at fracture origins compared with other billets tested in this period and previously.<sup>21,8</sup> Also, the average fracture strength was ~10 Kpsi higher than other billets fabricated with alum derived powder. Exaggerated grain growth was the dominant flaw. However, the size of the larger grains was not markedly greater than the matrix. This undoubtedly accounts for the closeness of the average strength for the flawed and unflawed groups. Figure 15 illustrated the flaw and fracture origin of a specimen originally in an "uncertain" category. This series of micrographs clearly reveal an unusual 20  $\mu m$  long rod (or plate) shaped grain along with several smaller but similarly shaped grains. This structure is not typical of exaggerated grain growth in  $Al_2O_3$ , thus it was concluded that the rod grains were either an impurity inclusion or  $Al_2O_3$  grain development caused by an impurity. The major defect in this billet was exaggerated grains. This may result from one of several causes; 1) the statistics of secondary grain growth, 2) incomplete distribution of the grain growth inhibitor, or 3) solid solution or fine particulate impurity phases which promote grain growth. If either (1) or (3) are the cause of this growth, the chances of correcting the defect using secondary powder processing is poor. Cause (2) could be corrected through improved mixing of the grain growth inhibitor. It is clear that the powder handling techniques instituted resulted in a significant improvement over employing "as-received" powder from the same vendor.<sup>28</sup>

The Bayer process powder from Vendor IV resulted in the lowest strength billet studied in recent years.<sup>2</sup> This would not have been predicted based on the average microstructure. However, a microstructural analysis for flaws did reveal problems (Figure 9). The same defect type found in the microstructural analysis was found at two fracture origins in the bend specimen. Figure 16 illustrates this in specimen 1940-5. Clearly, volume flaws can cause fracture in  $Al_2O_3$ . This flaw was approximately 60  $\mu m$  below the tensile surface. The nominal stress at this level is 48.5 Ksi, some 2.7 Ksi below the calculated outer fiber stress. This lenticular defect probably develops during evaporation of an impurity. Clearly, material with this large a defect would be unacceptable for most structural applications.

TABLE IV  
Fracture Strength and Flaw Analysis

Powder Vendor, Specimen, and Test Condition	Bend Strength Kpsi	Observation
<u>Vendor II</u>		
<u>1007 + 23°C Ambient</u>		
-1	87.7	Possible large grain or transgranular patch.
-2	89.2	Center fracture origin - no flaw located.
-3	59.8	Corner fracture origin at large grain.
-4	87.3	Near corner fracture origin - no flaw located.
-5	70.4	Impurity related structure at origin.
-6	88.4	Center fracture origin - no flaw located.
-7	64.7	Center fracture origin - no flaw located.
-8	73.6	Center fracture origin - no flaw located.
-9	69.0	Center fracture origin - no flaw located.
Average	76.7 ± 11.5	
<u>Vendor IV</u>		
<u>1940 + 23°C Ambient</u>		
-1	53.0	Possible large grain or transgranular patch.
-2	52.4	Black particulate impurity at origin.
-3	59.3	Large grain at origin.
-4	55.8	Horizontal scratch on radius at origin.
-5	51.2	Lenticular impurity related pore at origin.
-6	56.1	Corner fracture origin - no flaw located.
-7	47.4	Lenticular impurity related pore at origin.
Average	53.6 ± 3.9	

TABLE IV cont.

Powder Vendor, Specimen, and Test Condition	Bend Strength Kpsi	Observation
<u>Vendor V</u>		
<u>1907 + 23° Ambient</u>		
-1	71.4	Center origin - no flaw located.
-2	90.1	Fracture origin at possible large grains.
-3	73.6	Fracture origin at metallic particle.
-4	83.2	Center origin - no obvious flaw - black defect nearby.
-5	74.4	Fracture origin at metallic particle.
-6	84.8	Corner flaw origin - metallic particle - many pieces.
-7	70.3	Fracture origin at metallic particle.
Average	78.3 ± 7.1	
<u>Vendor VI</u>		
<u>1417 + 23°C Ambient</u>		
-2	81.2	Particulate impurity at fracture origin.
-3	68.3	10 µm grain at fracture origin.
-4	76.5	Corner fracture origin and chip missing preventing thorough examination.
-5	86.6	Fracture origin not located.
-6	89.2	Transgranular region at fracture origin - uncertain if flaw is present.
Average	80.4 ± 7.5	
<u>1206 + 23°C Ambient</u>		
	61.7	Black filament near fracture origin. Possible large grains at origin.
<u>1231 + 23°C Ambient</u>		
	65.6	Corner fracture origin - no flaw located.
Average	63.6	

TABLE IV concluded

<u>Powder Vendor, Specimen, and Test Condition</u>	<u>Bend Strength Kpsi</u>	<u>Observation</u>
<u>Vendor VI</u>		
<u>1326 + 23°C Dry</u>	101.4	Corner fracture origin - no flaw located.
<u>1331 + 23°C Dry</u>		
-1	97.9	Subsurface particulate at fracture origin.
-2	91.5	Corner fracture origin - no flaw located.
<u>1337 + 23°C Dry</u>	82.5	Center fracture origin - no flaw located; however, linear flaw near origin.
Average	<u>93.3 ± 7.2</u>	

TABLE V  
Summary of Flaw Analysis

<u>Billet</u>	<u>No. of Tests</u>	<u>No Flaws Detected</u>	<u>Large Grains</u>	<u>Particulate Inclusion</u>	<u>Machining Scratch</u>
Vendor II - 1007	9	6	2	1	
Average Strength, Ksi	76.7	77.5	73.7	70.4	
Vendor IV - 1940	7	1	2	3	1
Average Strength, Ksi	53.6	56.2	56.1	50.3	55.8
Vendor V - 1907	7	2	1	4	
Average Strength, Ksi	78.3	77.3	90.1	75.8	
Vendor VI - 1417	5	3	1	1	
Average Strength, Ksi	80.4	84.1	68.3	81.2	
Vendor VI - 1326, 1331 at 23°C Ambient	2	1		1	
Average Strength, Ksi	63.6	65.6		61.7	
Vendor VI - 1326, 1331, 1337 at 23°C Dry	4	3		1	
Average Strength, Ksi	93.3	91.8		97.9	
Frequency of Occurrence in Total Testing, %		47.0	18.7	34.3	3.0



12

(a)

10X



13

(b)

800X

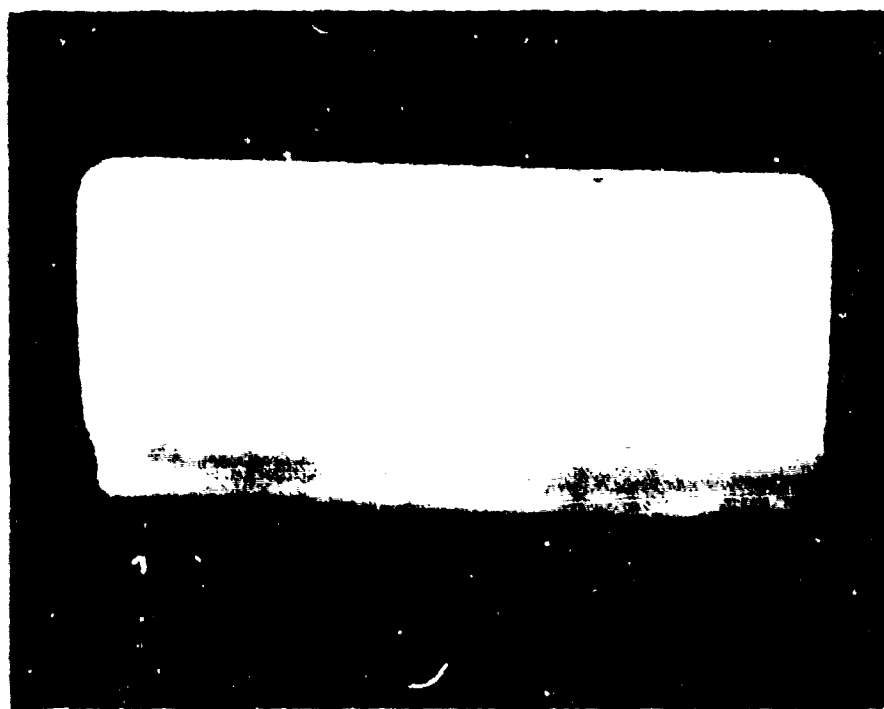


14

(c)

4000X

Figure 15. Specimen 1947-5 showing (a) surface of film, (b) medium magnification view of the grain structure, and (c) high magnification view of the grain origin.



9% S-5

15X

Figure 10. Specimen 1960-7 showing lenticular pore at Fracture Origin.

Four out of the seven Vendor V-1907 bend specimens had particulate impurities at fracture origins. Particulate impurities were observed during the general microstructural analysis and were described as soft metallic brass inclusions. Figure 17 illustrates a SEM study of sample 1907-5. The flaw structure is a pit with an associated multigrain particle at a higher elevation than the plane of the fracture surface (confirmed by examining a stereo-pair). The structure of the raised particle is different than the matrix and several of the grains are elongated and have lines that could be slip lines. The results of a microprobe analysis of this defect are shown in Figure 18. The two scanning views (Figures 18a and 18d) clearly show the presence of a heavy element in the defect area. The secondary emission maps and accumulative counting trace clearly show the defect to be mainly Cu associated with what looks like discrete Fe rich particles. It is important to note that Al is absent in this area. One preliminary view was that unreacted Al was present in this powder. This view was never substantiated. The apparent size of the defect area is somewhat surprising when comparing Figures 17 and 18. There is some scattering which gives the impression of a larger contaminated area than actually present; however, the conclusion must be reached that the contamination extends to an area  $\approx$  the size of pit and particle shown in Figure 17c. This type of defect was the dominant strength limiting defect in this material. Given the high incidence of particulate impurities in this billet, the rather high 78.4 Ksi average strength is surprising. This suggests that this method of powder manufacture holds considerable promise for producing high strength structural  $Al_2O_3$  given a clean in-house processing operation.

The high purity undoped  $Al_2O_3$  billets from Vendor VI powder exhibited a strength/grain size relation in the order expected under ambient test conditions. The 1.25  $\mu m$  grain size billet (1417) had about 16 Kpsi higher strength than the 4.8  $\mu m$  grain size billets (1326 and 1331), which certainly appears reasonable for grain size controlled strength. It is interesting to note that the strength for specimen 1417-3 was reduced to the level of specimens 1326 and 1331 and a large grain of about 10  $\mu m$  was found at the fracture origin. The flaw analysis demonstrated that this powder had some incidence of flaw origins from particulates. Figure 19 shows the results of an SEM study on specimen 1331-1 which fractured at 97.9 Kpsi in a dry environment. The hole is 28  $\mu m$  below the surface and has a diameter of 7.5  $\mu m$ . The grain structure near the hole is somewhat larger than the matrix, suggesting that an impurity particle melted during consolidation, diffused into the surrounding structure, and affected grain growth in this region. Flaws were not found at the fracture origins of many specimens. A second specimen from Vendor VI powder examined by SEM was 1337-3, 80.5 Kpsi specimen fractured in argon. Figure 20 shows the entire fracture surface and fracture origin. A careful examination of this entire zone failed to find any obvious flaw, Figure 20b. The structure near the surface was judged to be transgranular fracture rather than a large grain. The low incidence of impurity flaws in these Vendor VI specimens was undoubtedly due in part to the purchase of a high purity powder and care in handling.

#### E. Discussion

Microscopy demonstrated that alum and nitrate derived powder had quite similar powder morphologies. This suggests that the decomposition route and phase transitions through the transitional  $Al_2O_3$  phases are

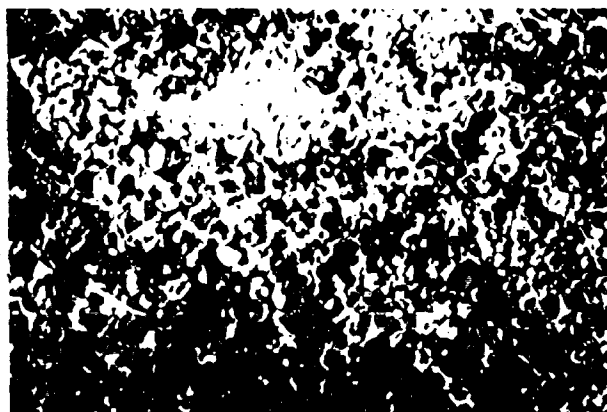




15E

(a)

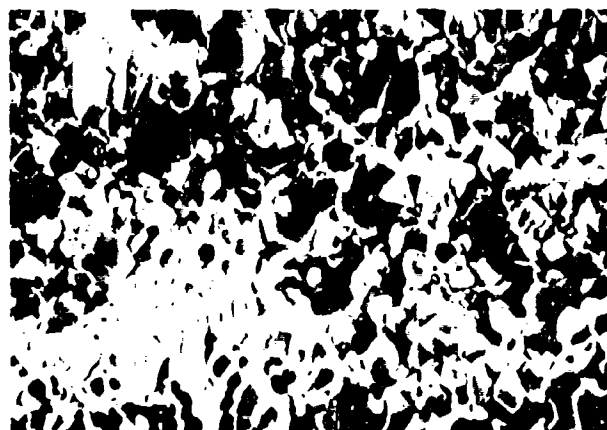
16X



16E

(b)

800X

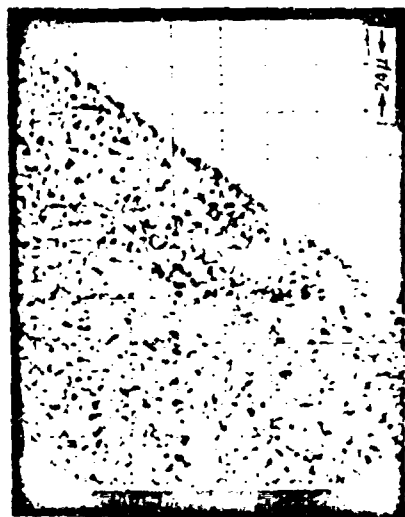


18E

(c)

1000X

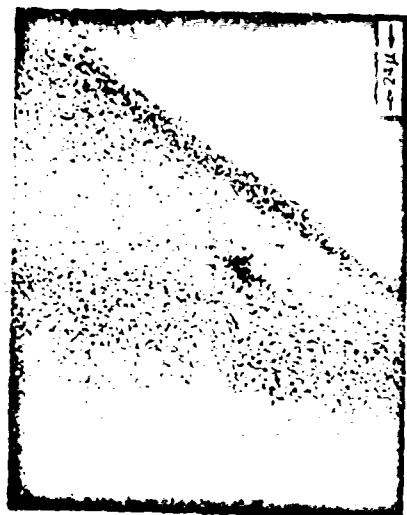
Figure 17. Specimen 1904-5 showing (a) fracture origin near center of bar, (b) subsurface pit and particle, and (c) higher magnification view of defect.



(a)



(b)



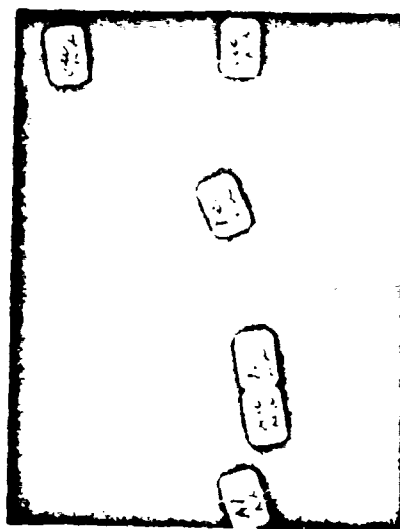
(c)



(d)

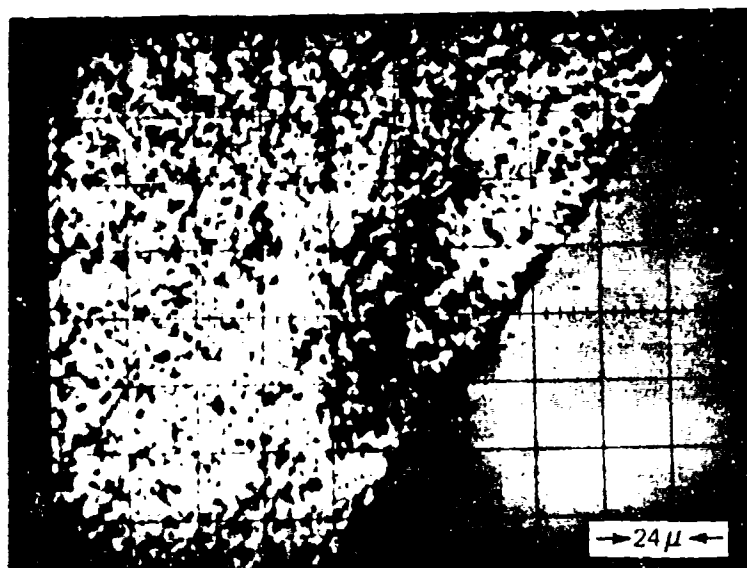


(e)

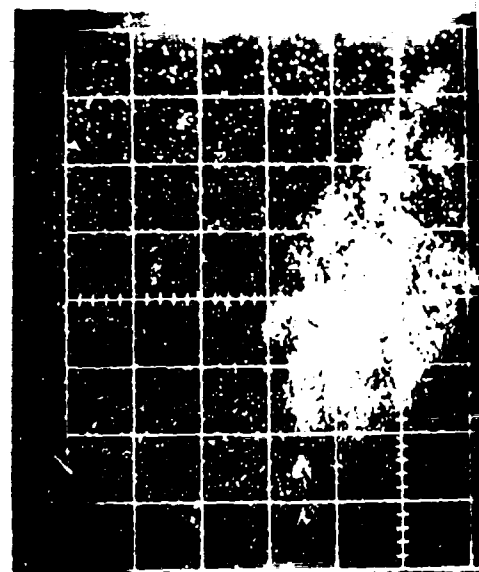


(f)

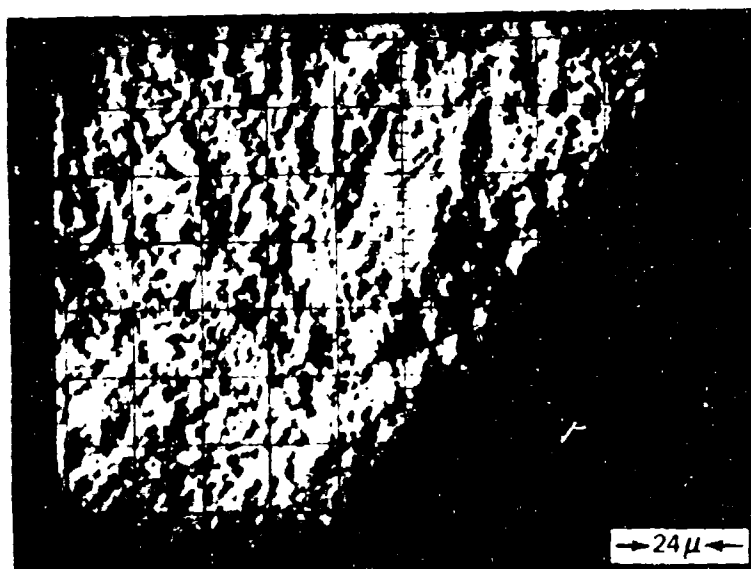
Figure 18. Microprobe study of fracture origin in Specimen 1907-5 showing (a) secondary emission of area around defect shown in Figure 17; (b) Cu emission; (c) Al emission; (d) backscattered X-ray emission (sample coated with Au and Pd); (e) secondary emission of area around defect shown in Figure 17; (f) Cu emission. See the following pages for greater detail.



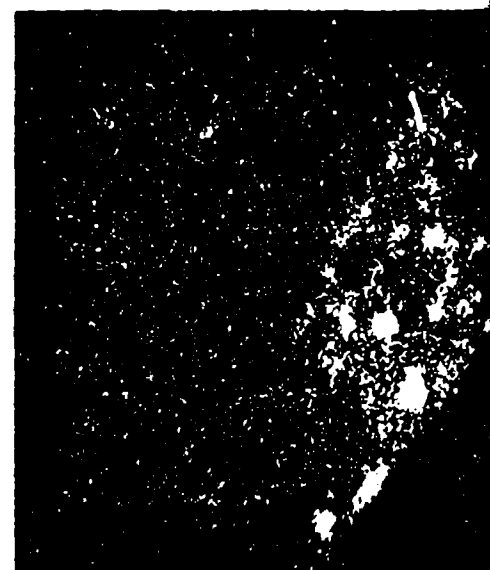
(a)



(b)

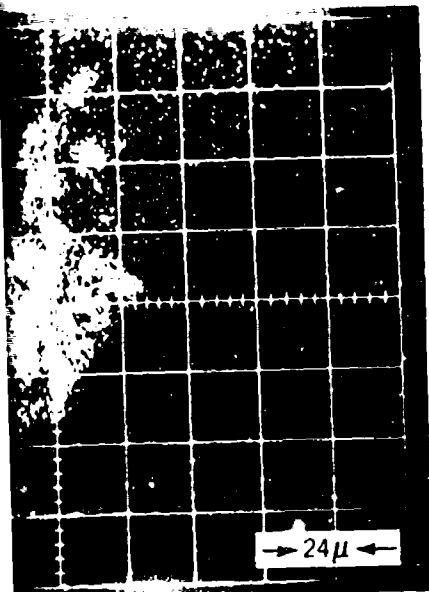


(d)

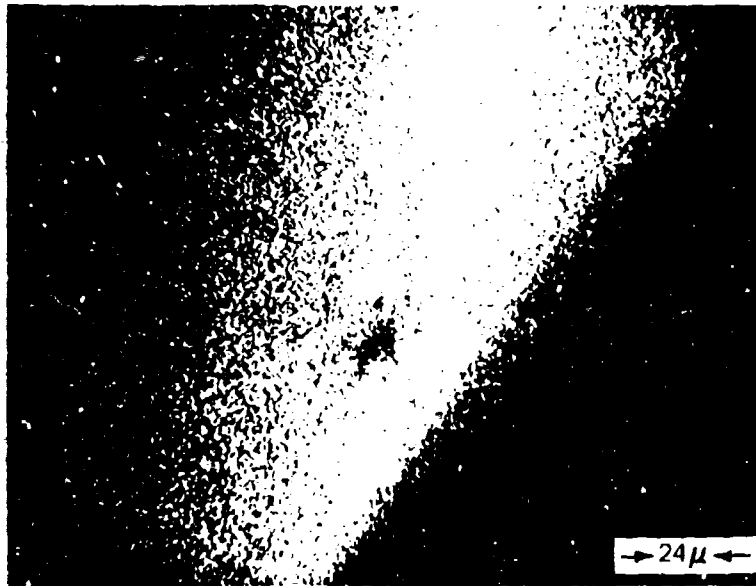


(e)

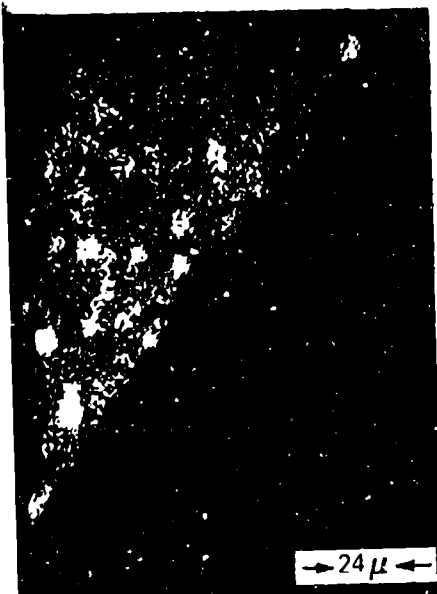
Figure 18. Microprobe study of fracture origin in Specimen 1907-5 showing (a) secondary emission; (b) Al emission; (d) backscattering from defect area; (e) Fe emission; and (f) acc



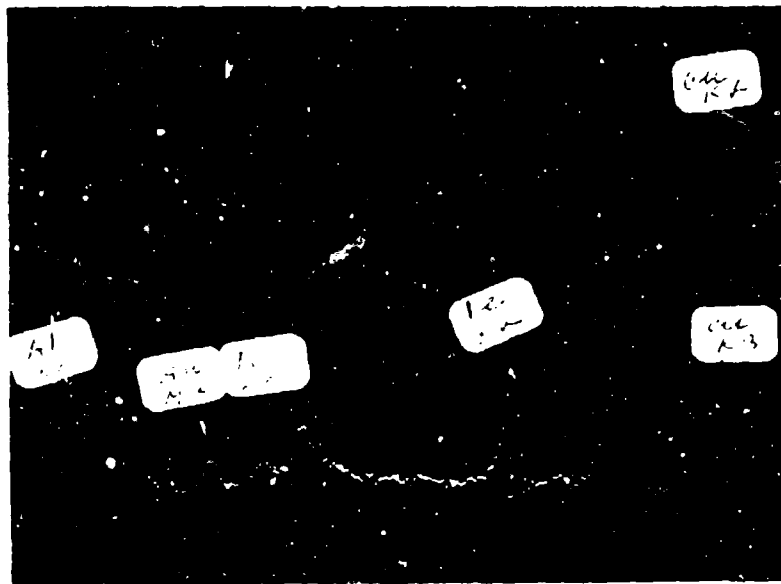
(b)



(c)



(e)



(f)

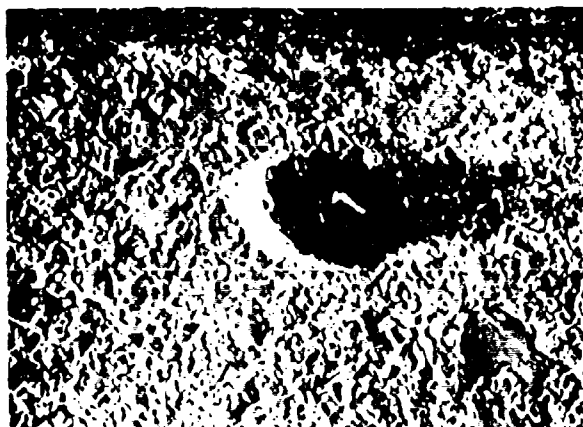
ary emission of area around defect shown in Figure 17: (b) Cu emission:  
 and (f) accumulative X-ray emission (sample coated with Au and Pd).



6

(a)

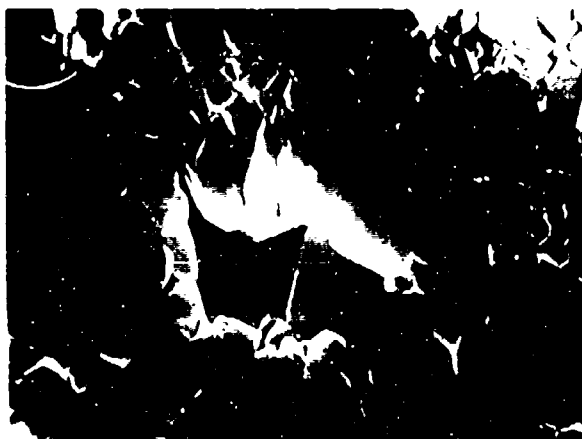
15X



7

(b)

750X



8

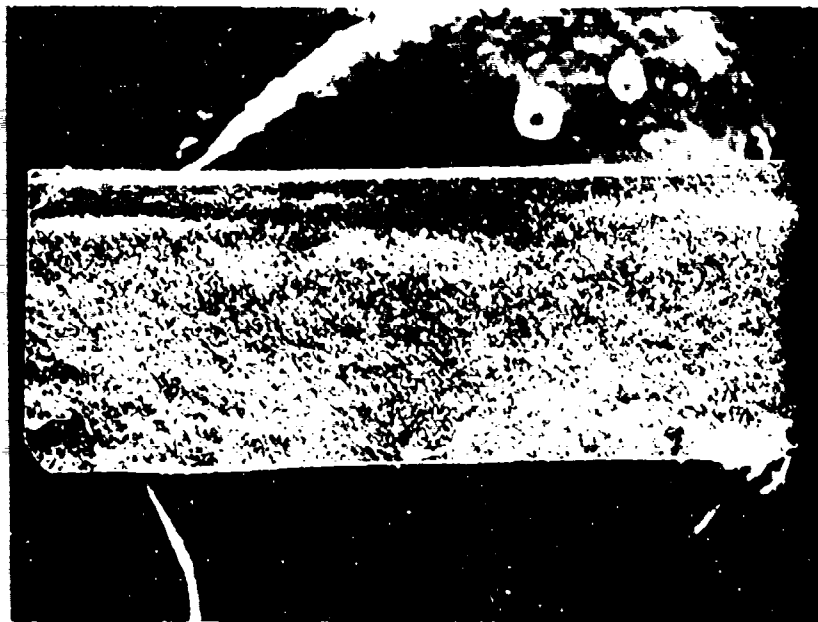
(c)

750X

Reproduced from  
best available copy.



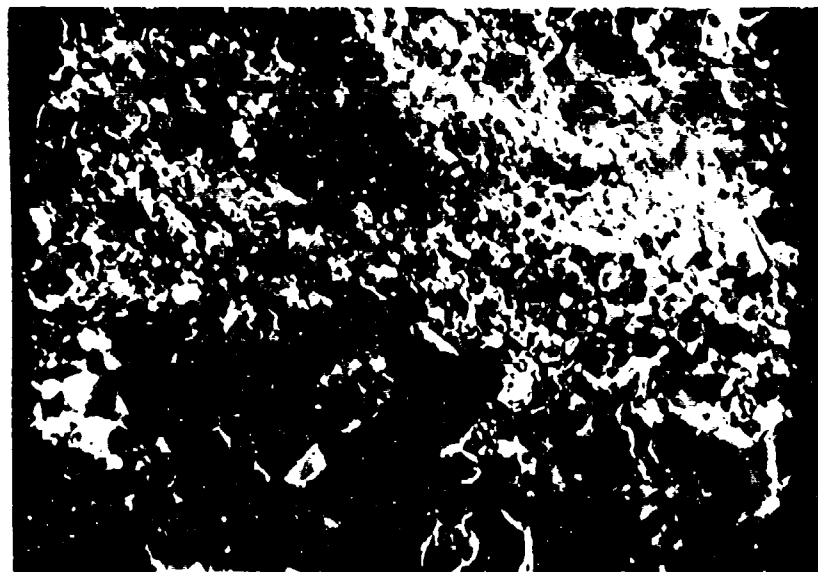
Figure 19. Specimen 1 (a) - fracture surface, (b) defect structure, and (c) defect structure (a) - fracture surface and exaggerated grain growth.



100X

(a)

100X



1000X

(b)

1000X

Figure 10. Fracture surface of 100-100-100 specimen showing (a) the crack surface, and (b) the granular structure at fracture origin.

similar. This would be an extremely interesting study from the mechanistic viewpoint. This similarity also suggests that highly active powders can be derived through a nitrate route rather than the more traditional alum route. This could eliminate the problems associated with retained O.

When Vendor II powder was processed in the "as-received" condition, the average bend strength was 62.3 Kpsi and 6 out of 8 bars had inclusions as fracture origins.<sup>28</sup> A special powder treatment to remove impurities resulted in a billet with an average strength of 76.7 Kpsi and 3 out of 9 bars with obvious defects as fracture origins. Since the in-house processing remained constant, this result is interpreted as strong evidence for strength limiting impurities being present in the "as-received" Vendor II powder.

The results for Vendor V powder are interpreted quite differently. In this case the powder analysis failed to reveal particulate impurities. However, the microstructure and fracture origins both showed the presence of a brass inclusion. Thus, in this case, it was judged that the powder was clean, but process errors introduced strength limiting defects. It is interesting and perhaps significant that the average strength of this material (78.3 Kpsi) was very close to that for the treated Vendor II material (76.7 Kpsi). It is possible that the strength of the treated Vendor II billet (1007) is now limited by process limitations. This statement is highly speculative as flaws were found in only 3 out of 9 fracture origins.

The Bayer derived powder, Vendor IV, although it appeared acceptable in a microscopic examination and an examination for particulate impurities, clearly gave an inferior hot pressed product. The cause of this was not traced down in detail. It is suspected, however, that colorless particulate impurities were present in the powder. During hot pressing a combination of reaction and volatilization gave some very large lenticular flaws.

Further support for the relationship between strength and powder purity came from the high average strength (80.4 Kpsi) for Vendor VI powder. This powder was purchased as a 99.9995%  $\text{Al}_2\text{O}_3$  grade, so it undoubtedly received special attention for cleanliness in the manufacturing process. The powder analysis revealed some problems with particulate impurities. However, as a result of the glove box handling procedures instituted for the in-house processing, there is reasonable confidence that no further contamination occurred. The strength gains over the Vendor II and V billets are very small, which is somewhat surprising and certainly discourages the widescale application of such elaborate handling procedures.

Figure 21 illustrates the interrelationships between strength and grain or flaw size (C in the Griffith equation) for the billets tested in this period compared with three commonly referenced<sup>6,7,8</sup> studies on strength/grain size relationships in  $\text{Al}_2\text{O}_3$ . The data plotted was specific flaw sizes (or half length for subsurface flaws) versus stress level (corrected for position from the tensile surface) and average strength data from specimens where no flaws larger than a grain size were detected. In this case the strength was plotted versus the billet grain size. The average

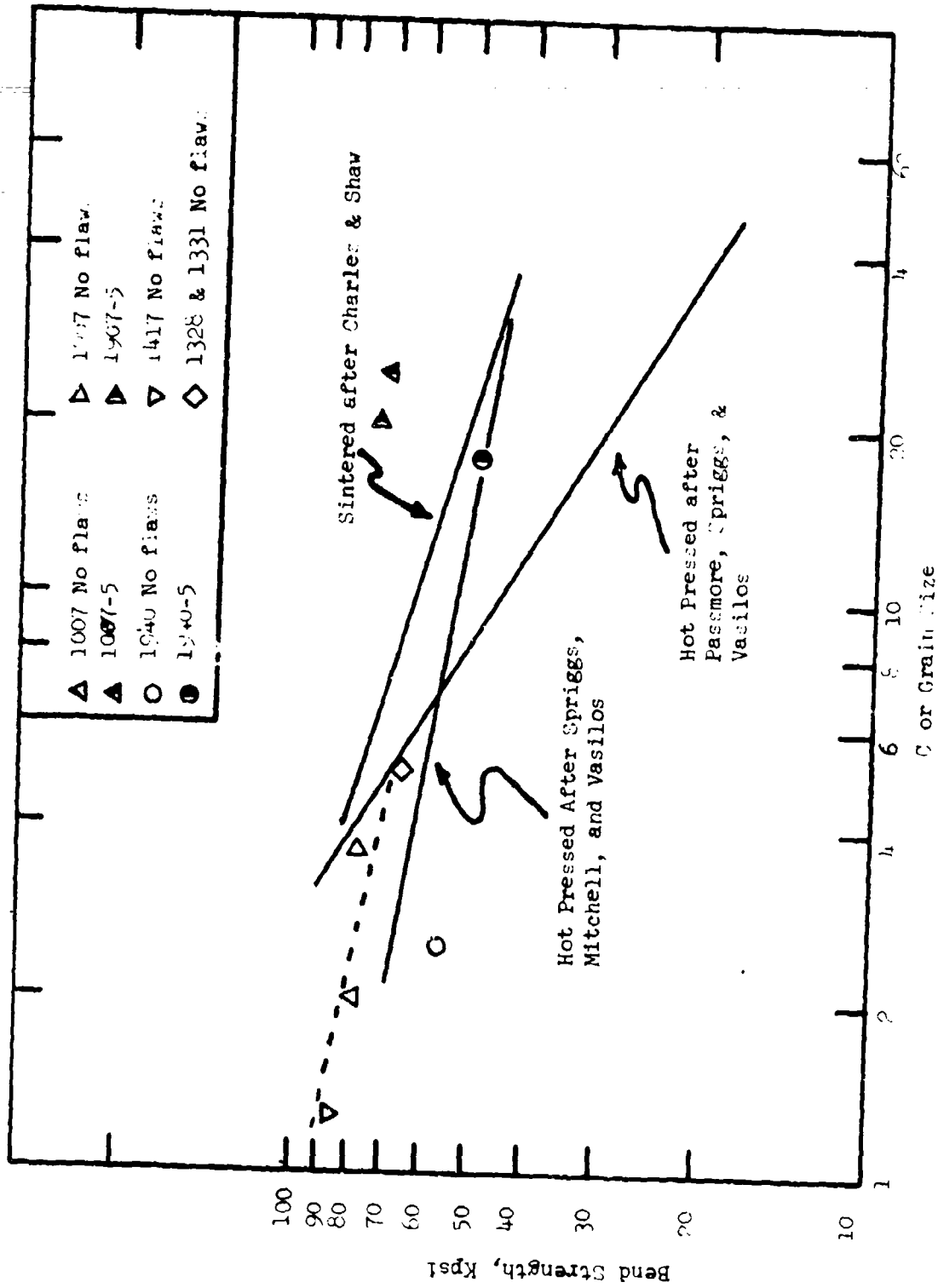


Figure 21. Room Temperature Bend Strength versus Grain Size or Flaw Size (Flaw size for internal flaws) compared with Literature strength-Grain size data.



strength data most closely follows the data of Spriggs et al.<sup>8</sup> A line (dashed) parallel and displaced to a higher stress than the Spriggs et al line fits four of these average strength points quite well. The average strength for 1940 was markedly below the dashed line, but curiously enough an extension of this line passes through the point for 1940-5. This suggests that the strength of billet 1940 is controlled by  $\sim 30 \mu\text{m}$  flaws even for the case where flaws were undetected. Consideration of the individual data points 1007-5 and 1907-5 suggest that there is some inherent strength advantage other than just a lower incidence and size of flaws for these billets over 1940. One possible explanation is that the fracture surface energy,  $\gamma_f$ , is lower for 1940 due to a lower grain boundary energy from an impurity argument.

The Griffith relation for a penny shaped flaw predicts that the fracture strength,  $\sigma_f$ , follows the relation

$$\sigma_f = \left( \frac{\pi E \gamma}{2(1 - \nu^2) C} \right)^{\frac{1}{2}} \quad (1)$$

where  $\sigma_f$  is the fracture stress, E the elastic modulus,  $\gamma$  the fracture surface energy, C the half length of the cross section of the crack, and  $\nu$  is Poisson's ratio. For an elliptical crack, this becomes

$$\sigma_f = \left( \frac{2 E \gamma}{\pi (1 - \nu^2) C} \right)^{\frac{1}{2}} \quad (2)$$

for the plane strain condition.

Alternately the Petch relation is of the form

$$\sigma_f = N(\sigma_y) + K G^{-\frac{1}{2}} \quad (3)$$

where  $N(\sigma_y)$  is a constant related to the yield stress, K is a constant, and G is the grain size. In addition to yield or micro-yield phenomena, Rice<sup>9</sup> and Kirchner et al<sup>5</sup> have attributed non-zero intercepts to thermal expansion anisotropy and elastic anisotropies.

All of the strength data where specific flaw sizes were detected and measured both in this study and previous studies<sup>2f,8</sup> were plotted in the Petch plot shown in Figure 22. Also shown is the best line for the hot pressed  $\text{Al}_2\text{O}_3$  data of Spriggs et al<sup>8</sup> as analyzed by Carniglia.<sup>10</sup> Specifically omitted from this plot are average strength data since this requires an assumption of flaw size.

When the data is treated in this way, no break appears in the Petch plot which implies that either equation (1) or (2) hold. This leads to the question of what causes the break in a Petch plot when data such as that of Spriggs et al are analyzed. It appears to the authors that a

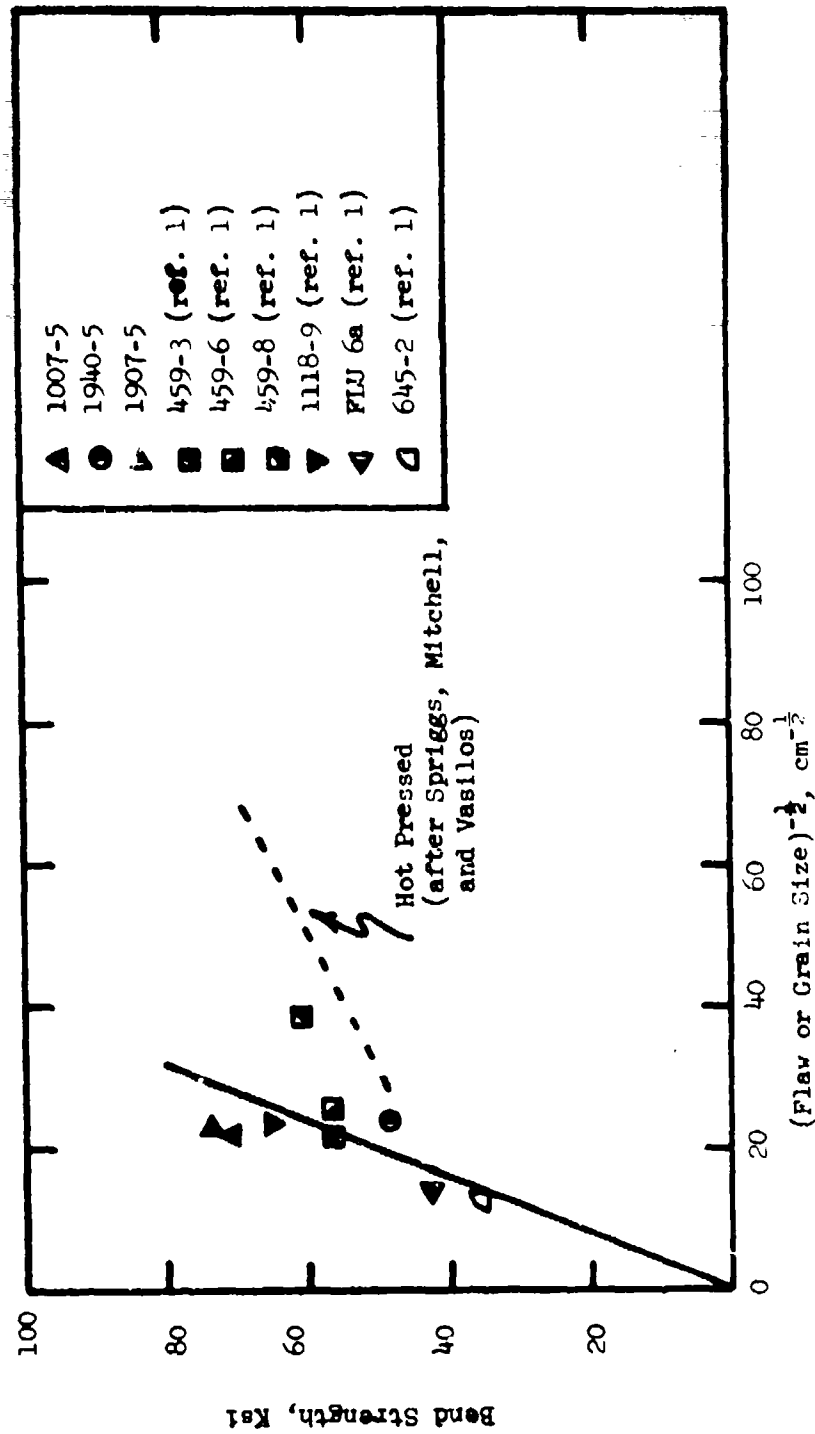


Figure 22. Room Temperature Bend Strength Versus Square Root of Inverse Flaw Size  
( $\frac{1}{2}$  flaw size for internal flaws)

major cause is the increasing C/G.S. ratio with decreasing grain size. At large grain sizes the flaws which in many cases are inherent to the powder employed are much smaller than the grain size. In this regime, surface damage to grains controls C. However, with reduced thermal cycles and smaller grain sizes, the inherent flaws start to dominate. At first there is competition between an inherent particulate related flaw and grain size related damage. This results in some positive slope to the Petch plot after the break. As grain size is reduced even further the inherent flaws dominate and strength remains constant with decreasing grain size. Examples of this response are evident in the recent review by Corniglia.<sup>10b</sup>

The slope of the solid line in Figure 22 must  $\approx \left( \frac{\pi E \gamma}{2(1 - \nu^2)} \right)^{1/2}$  for equation (1) and  $\left( \frac{2 E \gamma}{\pi (1 - \nu^2)} \right)^{1/2}$  for equation (2). Using the known

value of  $E = 59.5 \times 10^6$  psi ( $4.09 \times 10^{11}$  N/m<sup>2</sup>) and  $\nu = 0.2$ , the effective  $\gamma$  can be calculated. Values of  $\gamma = 4.44$  J/m<sup>2</sup> and  $10.92$  J/m<sup>2</sup> are obtained from the penny and elliptical crack solutions, respectively.

Collected in Table VI are effective surface energies calculated from the literature in a similar manner to that shown above, some values calculated on specific bars tested in dry or liquid nitrogen environments, values measured directly by Weidernhorn<sup>11</sup> on single crystals, and a number of investigators<sup>12,13,14</sup> on polycrystalline Al<sub>2</sub>O<sub>3</sub>.

Examination of this table shows that the calculated  $\gamma_f$  from Figure 22 fall between the chemical surface energy ( $\sim 1$  J/m<sup>2</sup>) and the polycrystal values when real flaws are taken into account. If the flaws are best approximated as elliptical flaws, the calculated  $\gamma_f$  comes very close to the single crystal values of Weidernhorn.<sup>11</sup> It is interesting to speculate on the meaning of this number, particularly since it is lower than most of the  $\gamma_f$ 's calculated for polycrystalline material. The  $\gamma_f$  calculated from the slope of Figure 22 probably represents a  $\gamma_f$  for initiation rather than propagation. Thus, possibly the  $\gamma_f$  represents the energy to propagate a crack through one or only a few grains. Such a process may reflect an energy closer to the single crystal values than the polycrystal values where literally millions of grains are either traversed (transgranularly) or circumvented (intergranularly). This view then postulates that a plot of  $\gamma_f$  versus C (instantaneous) would start at the single crystal value and stay at this level for  $C \ll 4$  G.S. The curve would then inflect upward and level off at a  $\gamma_f$  representative of the observed polycrystalline values.

There are at least two other explanations for low  $\gamma_f$  values. The flaws in many of the bars plotted in Figure 22 were apparently associated with chemical impurities. Grain boundary energies in the vicinity of the flaw may therefore be significantly lower from chemical effects. Consequently, the energy to extend cracks would be lower, accounting for the low  $\gamma_f$ . Stress concentrations may also be associated with the flaws plotted in Figure 22. The presence of such a concentration could allow a crack to extend more easily than the inherent resistance of the material would predict, giving rise to an apparent low  $\gamma_f$ .

TABLE VI  
Calculated and Measured Fracture Surface Energies

<u>Data</u>	<u>Test Condition</u>	<u>Fracture Surface Energy</u>	
		<u><math>\gamma</math> Penny</u>	<u><math>\gamma</math> Elliptical</u>
Data of Figure 22	23°C Ambient	4.44	10.92
1331-1	23°C Dry	2.53	6.24
1118-13	-196°C N <sub>2</sub>	9.20	22.6
Charles & Shaw	23°C Ambient	5.32	13.16
	-196°C N <sub>2</sub>	8.90	22.2
Weiderhorn <sup>11</sup> (single crystal measured)	23°C Dry	7.3 prism	
		6.0 rhombohedral	
Swanson <sup>12</sup> (polycrystal measured)		24.3 - 3 $\mu$ G.S.	
Gutshall & Gross <sup>13</sup> (polycrystal measured)		18.2 - 10 $\mu$ G.S.	
Simpson <sup>14</sup> (polycrystal measured)		45 - 1 $\mu$ G.S.	

Table VI shows that lower temperatures raise  $\gamma_f$  as expected from bond strength considerations. It is interesting that the internal flaw on sample 1113-1 (tested dry) gave only a slightly higher  $\gamma_f$  than the Figure 22 plot, indicating a small effect of moisture on  $\gamma_f$ .

The observed  $\gamma_f$  is sufficiently high, however, that a back calculation into equation (2) predicts strengths of 112 Kpsi, 176 Kpsi, and 250 Kpsi for material with flaw sizes of 5  $\mu$ m, 2  $\mu$ m, and 1  $\mu$ m, respectively. The challenge to produce this material is clear, and it is our desire that this work has to some extent given guidance to this endeavor.

#### F. Conclusions

1. Of the four grades of  $Al_2O_3$  powder employed, only one did not contain particulate impurities in the "as-received" condition.
2. Particulate impurity contamination was significantly reduced by an in-house treatment.
3. Processed billets contained two major defects; large grain size zones and particulate inclusions. The latter defect was the most serious in limiting strength.
4. Fifty percent of the fracture could be traced to a defect in the material. Flaws could not be found at fracture origins in 47% of the bars tested, while the remaining 3% could be ascribed to a machining error.
5. A Petch plot can have a non-zero intercept due to the increasing crack/grain size ratio with decreasing grain size. Thus, although microplastic effects are acknowledged as being important in some systems, a non-zero intercept should not, without examination of fracture origins, be considered proof of plastic or anisotropy related fracture initiation.
6. Fracture surface energies calculated from a Griffith relation where flaw sizes were known fall between the chemical surface energy and single crystal fracture surface energy. This was thought to represent a more realistic value of the crack initiation process than recent direct measurements on polycrystalline  $Al_2O_3$ .

### III. PRESS FORGING

#### A. General

It has previously been established that high density bodies with unique properties can be achieved by press forging polycrystalline  $Al_2O_3$ .<sup>2</sup> High in-line optical transmissivity can be obtained as a result of nearly complete pore removal and strong crystallographic texturing. The textured structure is achieved by plastic deformation primarily on the basal slip system. This texture is retained through primary recrystallization.

Porosity distributed throughout the structure may act as preferred

nucleation sites for the new generation of grains during recrystallization. This process itself could absorb porosity or the structure could be more susceptible to continued densification due to the nearness of pores to grain boundaries; their potential sink. In-line light transmissions of 50% at 0.55  $\mu$  wavelength were achieved for the forged material as compared with a maximum of 15% for the best randomly oriented pore-free  $Al_2O_3$  available at an equivalent thickness. This resulted from the preferred basal texture eliminating to a large extent the light diffraction due to birefringence. Inverse pole figures demonstrated that the crystallographic orientation was strong but not perfect. The misorientation undoubtedly accounts for the absence of even higher optical transmission figures.

Mechanical strength was the second property that was enhanced as a result of forging. It was found that the strength at  $-196^\circ C$  and  $1700^\circ C$  was nearly independent of grain size in the 1-20 micron range<sup>2a, b</sup>. Fracture strengths in the  $1200^\circ$  to  $1450^\circ C$  range were over 50% higher than straight hot pressed material of an equivalent grain size<sup>2c</sup>. However, there was no apparent effect of texture on the plastic properties between  $1475^\circ$  -  $1700^\circ C$ .<sup>2b</sup>

More recently, thin shell 2-inch and 3-inch diameter hemispheres have been forged which retain the crystallographic orientation in the plane of the shell<sup>2f, g</sup>. The optical transparency has been nearly uniform throughout the full hemisphere on the best samples; however, regions of low transmission or excessive haze remained a problem in many forgings. During forging of the sintered preforms, edge tears often developed in the skirt of the forging and some of these extended through the 0.4-inch skirt into the hemispherical portion of the forging. The tearing was thought to be caused by cavitation resulting from a more rapid deformation than the available mechanisms could accommodate at the imposed strain rate. Finally, some problem with reaction, possibly involving the BN parting media, can be a problem at high forging temperatures and relatively long times; this counters the improvements in optical properties which usually result with higher forging temperatures. A recent series of experiments indicated that the edge tearing could be eliminated using powder preforms.<sup>2e</sup> However, these forgings consistently had low optical transmission which presumably resulted from a combination of the higher residual porosity because of the short hold times employed to eliminate any reaction and perhaps also from the higher CO content compared to the preforms sintered to the closed pore stage in  $H_2$  which is much more soluble in  $Al_2O_3$ .<sup>15, 16</sup>

Most recently it has been demonstrated that  $Si_3N_4$  can be successfully press forged using similar techniques as for  $Al_2O_3$ .<sup>2g</sup> A crystallographic texture develops which is opposite that in  $Al_2O_3$  in that the "c" axis tends to align itself perpendicular to the pressing direction; a pronounced microstructural texture was also apparent. These preliminary forgings still had higher porosity levels than are usual for hot pressed  $Si_3N_4$  and the strengths of the forged billet were below those of good hot pressed material. A 2-inch diameter hemisphere was also forged from a  $Si_3N_4$  powder preform demonstrating the utility of forging for forming shapes of  $Si_3N_4$ .

#### B. Raw Materials and Preforms

Vendor III 99.98%  $Al_2O_3$  powder was used for the hemisphere forging

experiments. Concentrations between 0.015 and 0.025 weight percent MgO were added to an alcohol/alumina slip in a ball milling operation. The dried powder was isostatically pressed at 30 Kpsi into cylinders 3 inches diameter by 4 inches long. These were cut and shaped in the green state into circular right cylinders 3-inch diameter by  $1\frac{1}{2}$ -inch high with a 2-inch radius cap. Some of the preforms were used in the green state while others were fired in  $H_2$  at  $1400^\circ - 1450^\circ C$ . After sintering, the preform dimensions are about 1-inch high with a diameter of 2.5 inch or less. The low MgO concentrations were selected to avoid the spinel second phase which had been observed in forgings with as little as 0.035% MgO and which apparently reduces the optical transmission.<sup>28</sup>

For the  $Si_3N_4$  disc forgings, powder preforms were used which were  $\frac{1}{2}$  inch in diameter and  $1\frac{1}{2}$  to 2 inch high. These were made from a high  $Si_3N_4$ - $Si_3N_4$  powder\* with a MgO additive which was ball milled in tertiary butanol using WC balls. The forging preforms were made directly by uniaxially cold pressing the dried powder at 7,500 psi without a binder; the green density was 1.53 g/cc (48% of theoretical).

### C. Press Forging Procedure

Forging runs were conducted in an induction heated 75 ton press using standard ambient graphite base hot pressing furnace construction techniques. The hemisphere forging die was constructed from high strength HFD Poco graphite. The material nearly matches the thermal expansion coefficient of  $Al_2O_3$ . This turns out to be an advantage in die design as dimensions can be directly translated. Also, problems of specimen/die thermally induced cool down constraints are greatly minimized using Poco graphite. The die was designed to produce a 1.52-inch radius hemispherical cap end with a 0.4-inch high  $8^\circ$  tapered cylindrical skirt. A pinned top ATI punch was used which allowed hot extraction of the male die. The boron nitride die lubricant was sprayed or painted directly onto the graphite. Ambient atmosphere forgings were employed which meant that at the forging temperature the atmosphere was predominantly CO with a partial pressure of  $CO_2$ ,  $H_2$ , and  $N_2$ . The argon permeated into the cavity from the sight tube where it was employed as a sight tube flush.

The die assembly was heated to the forging temperature in about 100 minutes. The ram travel was initiated and driven by a manual strain rate control. The strain rate during the rapid deflection regime was controlled to between  $2 \times 10^{-4} \text{ sec}^{-1}$  and  $1 \times 10^{-3} \text{ sec}^{-1}$  by continually changing the deflection rate. This represents the best present estimate of acceptable strain rate in the  $1850^\circ C$  range. Once maximum pressure was reached, the deflection rate slowed down as forging and densification came to a conclusion. After measurable deflection ceased, the temperature was reduced from  $1875^\circ C$  to  $1825^\circ C$  and the billets were held for 2 to 3 hours to achieve additional densification which in the final stage takes place by diffusion; there is some evidence that an additional recrystallization may take place during this period;<sup>17</sup> the reduced temperature was used to prevent surface reaction and sticking during the long hold times. Upon completion of the run, pressure was reduced and the male punch retracted

---

\*Advanced Materials Engineering Ltd.

before cooling.

The  $\text{Si}_3\text{N}_4$  upset forgings were done in a 3-inch graphite die with flat punches. To prevent reaction and sticking, the punch faces were coated with a layer of BN or with a 0.010 thick piece of Mo foil which was then coated with PN. Initial pressure for all these forgings was applied at  $1650^\circ$  or  $1705^\circ\text{C}$  with a target strain rate of about  $3 \times 10^{-4} \text{ sec}^{-1}$ ; heating to the final temperature was continued during the early part of the forging, and when full pressure was achieved the piece was held for 1-2 hours to achieve further densification. At the pressures employed, the pieces typically flow out until they contact the die wall, but complete corner fill is not achieved.

#### D. Textural Analysis

The texture or degree of crystallographic orientation in forged materials is best determined by X-ray diffraction techniques. Such information, of course, is of great benefit in the interpretation of the forging studies. Texture is completely described by the construction of a pole figure which shows the distribution of the orientations of the various crystallographic axes of the individual crystallites in the polycrystalline body relative to the axes of the forging process. However, for the purpose of evaluating relative degrees of orientation, a simpler system was devised which is used on 3/8-inch square specimens taken from forged billets.

The diffraction pattern of a random (powder) sample was obtained. Values of  $f_0(I_{hkl})$  or normalized intensities defined by the relation

$$f_0(I_{hkl}) = \frac{I(hkl)}{\sum_{h,k,l} I(hkl)}$$

were calculated for each of a number of reflections from planes at various angular orientations with respect to the basal plane.

Similarly, values  $f(I_{hkl})$  were calculated from the diffraction pattern of a flat ground surface on a forged specimen. The ratios of the normalized intensities for the respective reflections  $R(I_{hkl}) = \frac{f(I_{hkl})}{f_0(I_{hkl})}$

which give the relative intensity of reflection are calculated and plotted against the angle  $\phi$  between the planes (hkl) and the basal plane.

In the case of a random powder sample, R has the constant value of unity over the entire  $\phi$  range. In the case of a perfectly oriented sample, R is zero everywhere except at  $\phi = 0$  where it has some large finite value. In the case of a distribution of orientation, in general, R will decrease monotonically from  $\phi = 0$  to  $\phi = 90^\circ$ . The better the crystallites are aligned, the higher the intercept at  $\phi = 0$  and the steeper the drop with increasing  $\phi$ .

#### E. $\text{Al}_2\text{O}_3$ Hemisphere Forging Results

The  $\text{Al}_2\text{O}_3$  forging experiments are listed chronologically in



Table VII. The principle objective for this group was to eliminate the cracking and reaction problems which had troubled previous forgings and still achieve good die fill and density in order to obtain useful optical properties.

The first run, 1956, utilized a powder preform in order to minimize rim cracks. One of the main objectives of this run was to raise the level of transparency in a hemisphere forged in this manner. Limited success was achieved in that approximately 40° of the arc was very translucent and another 50° exhibited some translucency. The process adjustment which accounts for this improvement compared to earlier forgings of powder preforms is the long soak time at 1825°C. Pore removal at this point in the process is a result of diffusional processes as opposed to action resulting from plastic deformation occurring earlier in the cycle. A long circumferential crack projected over the apex on the outer surface. The crack was healed, however, as there was no evidence of the crack when the sample was viewed from the back. Thus, it appears that the crack formed early in the cycle and largely healed during the subsequent forging and densification steps. It is uncertain how deep the crack or damage from the crack extends. In all likelihood BN from the die wall has become entrapped in the structure as was noticed on a run several years ago.<sup>2f</sup> Therefore, this condition must be avoided. The rim crack was well within tolerable limits as it did not come close to extending into what would be considered the full hemispherical shell. The control of rim cracks has been the main benefit from employing cold pressed preforms. Apparently the porosity allows a greater degree of accommodation during forging than is available in dense material.

The next two runs, 1975 and 1986, both used preforms which were pre-sintered to 81 and 90% of theoretical, respectively; at this stage the porosity is still open. For 1975 the pressure was initially applied at 1765°C while heating to the 1875°C forging temperature. Both pieces were crack free, as can be seen in Figure 23 which shows the as-forged hemisphere, 1986, and both pieces were free of reaction or sticking. Both had a high translucency over about the center 60° of arc with lower translucency away from the apex region; 1975 appeared somewhat more translucent than 1986. These forgings demonstrate that the careful strain rate control can provide sound forgings without either rim or apex cracks in initially porous preforms. The extended hold times at slightly reduced temperature were at least partially successful in providing increased densification and optical transmission, while eliminating reaction or sticking.

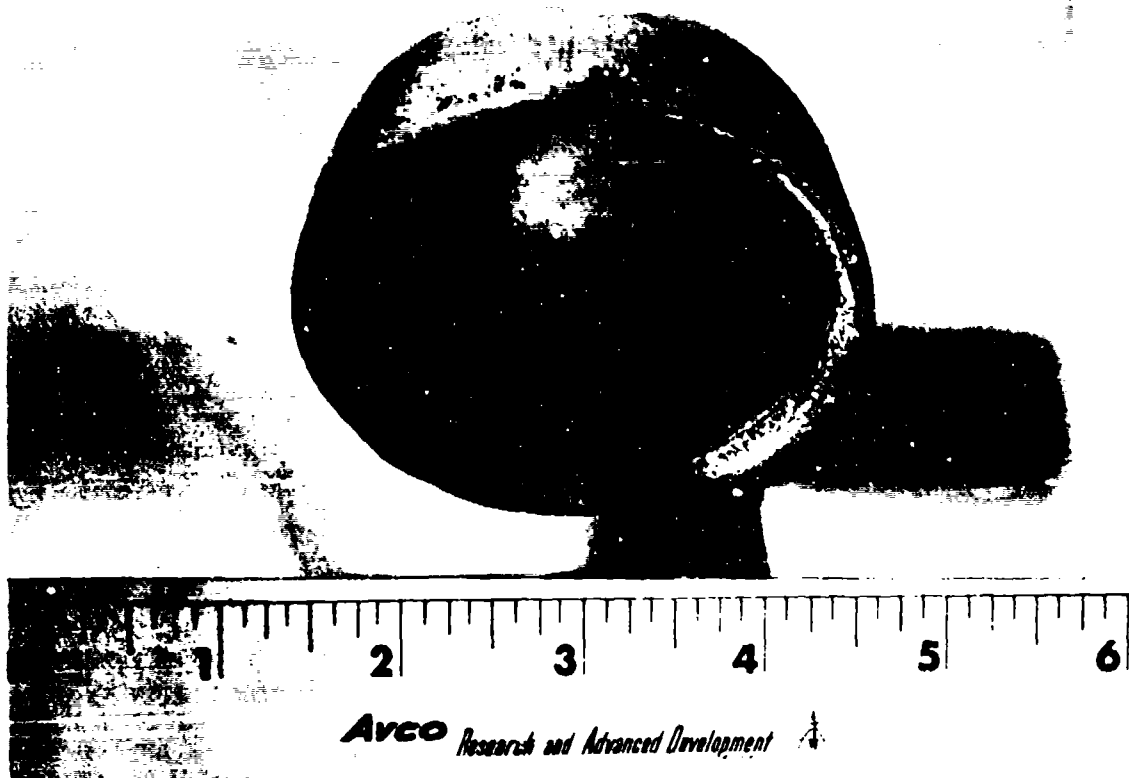
An additional annealing experiment was done on a previous hemisphere, 1838, which had been made from a preform sintered to 98.5% in H<sub>2</sub>. A piece was cut from the apex which had a density of 3.94 g/cc (compared to 3.85 g/cc for the entire hemisphere); the piece was annealed in vacuo at 1850°C for 18 hrs. After annealing the density was 3.89 g/cc (97.6%), and in a region along the inner diameter covering about one third of the thickness the piece had changed from translucent to an opaque white. Although a similar loss in density during annealing without pressure was previously seen on a hemisphere made from a powder preform,<sup>2g</sup> it had not been expected in this case since the preform presumably had H<sub>2</sub> rather than CO in the residual pores and H<sub>2</sub> has a sufficiently higher solubility and diffusivity to allow sintering to theoretical density in it.<sup>15</sup> An examination

TABLE VII  
Hemispherical Al<sub>2</sub>O<sub>3</sub> Forging Experiments

Experiment	Powder	Preform Prep.	Preform Density gm/cc	Separating* Media	Temp. °C (corrected by 65°C)	Pressure psi	Time** min.	Density gm/cc	Remarks
1956	U-1 Al <sub>2</sub> O <sub>3</sub> 0.025% MgO	Cold Press	1.80	BN/BN	1875	6250	5 (65) 185	3.91	Translucent for 40° of arc. Healed apex crack. One 3/16" rim crack.
1975	U-1 Al <sub>2</sub> O <sub>3</sub> 0.025% MgO	Cold Press Sinter H <sub>2</sub>	3.22	BN/BN	1875 1825	6250 6250	35 (65) 145	3.93	Translucent for 60° of arc. No cracks. Initial pressure applied at 1765°C.
1986	U-1 Al <sub>2</sub> O <sub>3</sub> 0.015% MgO	Cold Press Sinter H <sub>2</sub>	3.61	BN/BN	1875 1825	6250 6250	30 (97) 180	3.93	Translucent for 60° of arc. No cracks.
1838 Vacuum Annealed	Apex from previous hemisphere	Cold Press Sinter H <sub>2</sub>	3.93		1850	0	1080	3.94 before 3.89 after	

\*Coating for female listed first.

\*\*The times in parenthesis are the total time at temperature, whereas the first times listed refer to time at temperature and pressure.



5890-1

1X

Figure 23. Forging 1986 from a presintered preform illustrating elimination of rim and apex cracks and reaction.

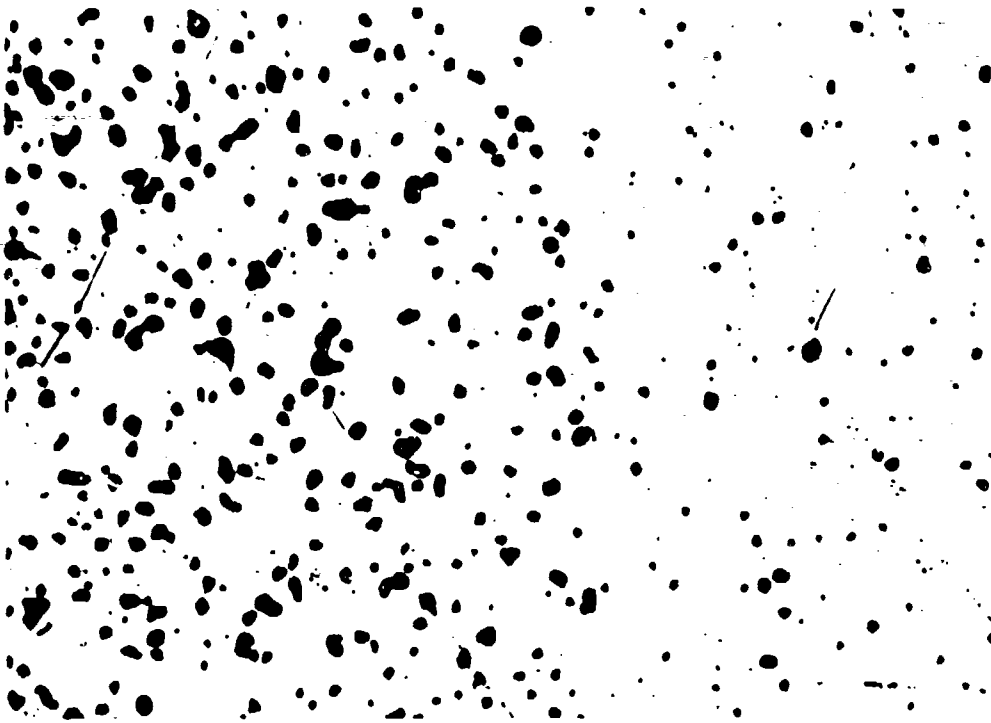
of the microstructure showed large, rounded pores as would be expected from a uniform pore coarsening and resultant bloating. However, two distinct regions could be seen in the specimen; near the inner face there was much more porosity than in the remainder of the cross section as shown in Figure 24; in addition, there were a few bloating cracks in this high porosity region. The cause of this is not fully understood, but it may indicate that early in the forging cracking occurs in some regions of the sample which is sufficient to allow introduction of CO into the pores. This CO would then cause high gas pressure in the subsequently sintered pores which would lead to bloating during annealing without an applied pressure. Near the outer surface, occasional patches of grains larger than 200  $\mu$  were occasionally found which are probably detrimental to the mechanical properties.

#### F. $\text{Si}_3\text{N}_4$ Forging Results

The  $\text{Si}_3\text{N}_4$  forgings are listed in Table VIII. All three were largely successful in that there was little or no cracking or sticking. There was, however, some edge cracking in two of the billets which has been a common occurrence in forgings of  $\text{Al}_2\text{O}_3$ .

The first forging, 1905, utilized only  $\frac{1}{4}\%$  MgO densification aid. Normally from 1-4% MgO is added, but a related program<sup>18</sup> established that 98% of theoretical density could be achieved with only  $\frac{1}{4}\%$  MgO. Further, it was shown that the high temperature bend strength is improved slightly at the lower concentration of MgO. This is thought to be related to a reduction in the amount of magnesium silicate grain boundary phase. This is important since the high temperature mechanical properties of hot pressed  $\text{Si}_3\text{N}_4$  are strongly influenced, if not controlled, by the grain boundary phase. This billet exhibited limited rim cracking and an overall density of 95.8% of theoretical. A piece from the center measured 99.7% of theoretical density indicating the presence of a low density rim which was confirmed by a microstructural examination shown in Figure 25. Also shown in this micrograph is interpenetration and reaction between  $\text{Si}_3\text{N}_4$  and what is assumed to be BN or a related phase; as long as such penetration is restricted to surface layers which can be removed by machining, it may be tolerable. The as-polished structure representative of the billets' interior is shown in Figure 26. The high density is confirmed by the micrographs. Also shown is a high reflectivity phase which is thought to be either FeSi or  $\text{Fe}_3\text{Si}$ . This phase is present in the AME high  $\alpha$ - $\text{Si}_3\text{N}_4$  powder and is common to most hot pressed  $\text{Si}_3\text{N}_4$ .

The next two billets had a 4% MgO additive. There was reduced edge cracking suggesting greater ductility results from the increased MgO, presumably as a result of an increased mass transport in a thicker grain boundary phase. The second of the two, 1973, was done at a higher forging temperature, 1865°C, which resulted in a further increase in ductility manifest by an elimination of edge cracks; this billet also had a slightly higher density, 99.1%, compared to 98.7% for 1972. The porosity in billet 1872 was not uniformly distributed, but instead, as seen in Figure 27, was in patches of coarse pores which are undesirable for strength considerations. The pores tended to be aligned in rows; however, these were not necessarily aligned normal to the forging direction. The origin of these is not certain; however, it is possible that they are a result of cracking



5868-2

100X

Figure 24. Microstructure of vacuum annealed piece of hemisphere 1838 showing coarse, partially spherodized porosity and two distinct regions with different porosity levels.

TABLE VIII

Si<sub>3</sub>N<sub>4</sub> Forgings

<u>Experiment</u>	<u>Powder</u>	<u>Separating Media</u>	<u>Temp. (Corrected by 65°C)</u>	<u>Pressure psi</u>	<u>Time* min.</u>	<u>Density g/cc</u>	<u>Remarks</u>
1905	Si <sub>3</sub> N <sub>4</sub> + 0.25% MgO	BN/BN	1805	5000	150 (190)	3.05	Limited edge cracking. Initial pressure applied at 1650°C.
1972	Si <sub>3</sub> N <sub>4</sub> + 4% MgO	BN-Mo/ BN-Mo	1805	4000	75 (107)	3.15	No sticking; minor edge cracks. Initial pressure applied at 1705°C.
1973	Si <sub>3</sub> N <sub>4</sub> + 4% MgO	BN-Mo/ BN-Mo	1865	4000	120 (160)	3.16	No sticking; sound, good billet. Initial pressure applied at 1705°C.

\*The time in parenthesis is the total time at temperature, whereas the first time is that at full pressure and temperature.



5808-1

100X

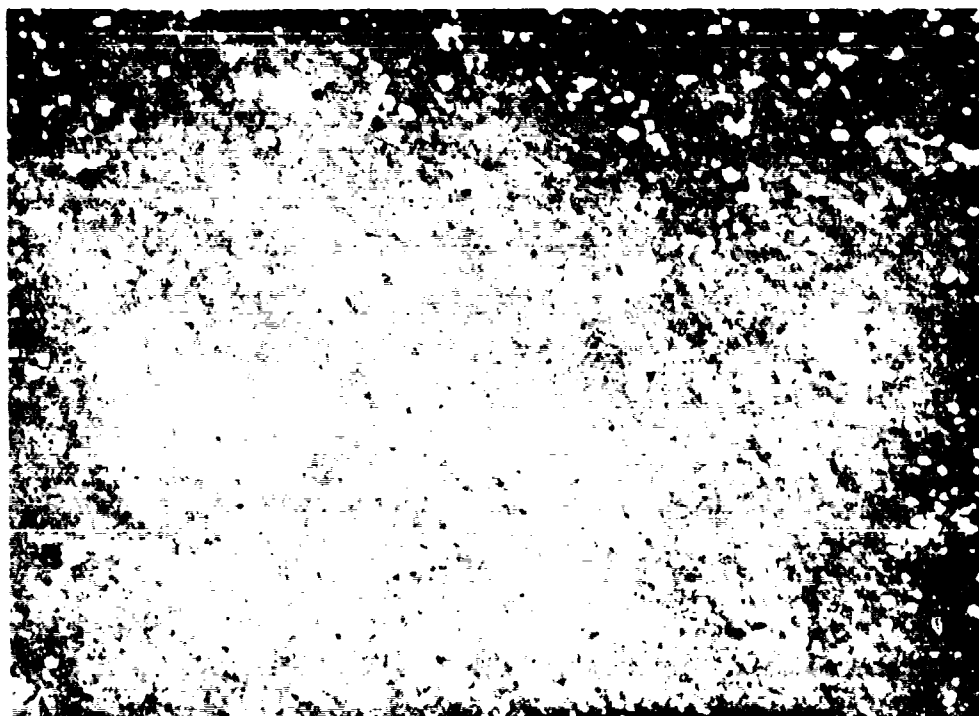
Figure 25. Rim Section of Forged  $\text{Si}_3\text{N}_4$ , Billet D1905 Showing Moderate Porosity and Interpenetration of BN or Related Phase.



5808-3

(a)

100X



5808-2

(b)

500X

Figure 26. Central Section of Forged  $\text{Si}_3\text{Al}_4$ , Billet B1905 Showing High Density and Iron Silicide Phase.





5869-3

100X

Figure 27. As-polished microstructure of forged  $\text{Si}_3\text{N}_4$ , 1972, showing regions of high porosity.

of the powder preform early in forging, or perhaps that they represent density variations remaining from the cold pressing. This porosity distribution is not observed in the hot pressed material.

X-ray diffraction analysis of billet 1905 revealed that  $\beta$ - $\text{Si}_3\text{N}_4$  was the major phase. One weak  $\alpha$ - $\text{Si}_3\text{N}_4$  diffraction line was present indicating a trace (1-5%) concentration. No diffraction lines were observed for the FeSi or related phase shown metallographically in Figure 26. A lineal analysis was performed on the metallographic section with the result that 3-4 vol. % FeSi (or related phase) was measured. This result is consistent with not finding this phase by X-ray analysis. An inverse pole figure orientation analysis was also performed. The results are shown graphically in Figure 28. The results are similar to those previously reported in terms of the orientation observed relative to the pressing direction ("c" axis normal to the pressing direction).<sup>28</sup> The degree of crystallographic orientation is somewhat higher than previously reported for a billet forged similar amount, but at slightly higher pressure and lower temperature.

Flexural strengths at room and elevated temperature were measured on billets 1905 and 1972. The tests were in 4 point bend using quarter point loading with a 0.050 x 0.100-inch cross-section and a 0.750-inch outer knife edge span. The high temperature tests were in argon and all were at a loading rate of about  $3 \times 10^3$  psi/sec. A few Charpy impact tests were also done on bars with a 0.250 x 0.250-inch cross section to compare with results on hot pressed  $\text{Si}_3\text{N}_4$  from another program.<sup>18</sup> The strengths, shown in Table IX, were better for billet 1905 than 1972. The superior low temperature strengths would be expected from the lower porosity and the better high temperature strengths both from lower porosity and lower MgO content. The strengths for 1905 indicated higher scatter than would be expected for good hot pressed material, suggesting there may be flaws from forging which can be eliminated to improve properties. The best strengths from 1905 are perhaps comparable with those from good hot pressed material. The impact strengths in the range of 3 to 4 in-lb are also comparable with those from hot pressed  $\text{Si}_3\text{N}_4$ ;<sup>18</sup> the value of 7 in-lb is the highest reported on any  $\text{Si}_3\text{N}_4$ ,<sup>18,19</sup> and so may indicate some promise for improved properties resulting from the strong microstructural texture which may be expected to contribute to a higher fracture surface energy.

#### G. Conclusions

1. Reduced cracking and reaction with increased optical transmission in forged  $\text{Al}_2\text{O}_3$  hemispheres using porous preforms could be achieved using careful strain rate control and a lower temperature annealing under pressure.
2. Forging of  $\text{Si}_3\text{N}_4$  can be used to produce crack-free bodies of good density. This process may be useful for producing shapes with strengths comparable to those achievable in high quality hot pressed bodies.
3. A strong crystallographic texture, with "c" axis perpendicular to the forging direction, results from forging  $\text{Si}_3\text{N}_4$ .

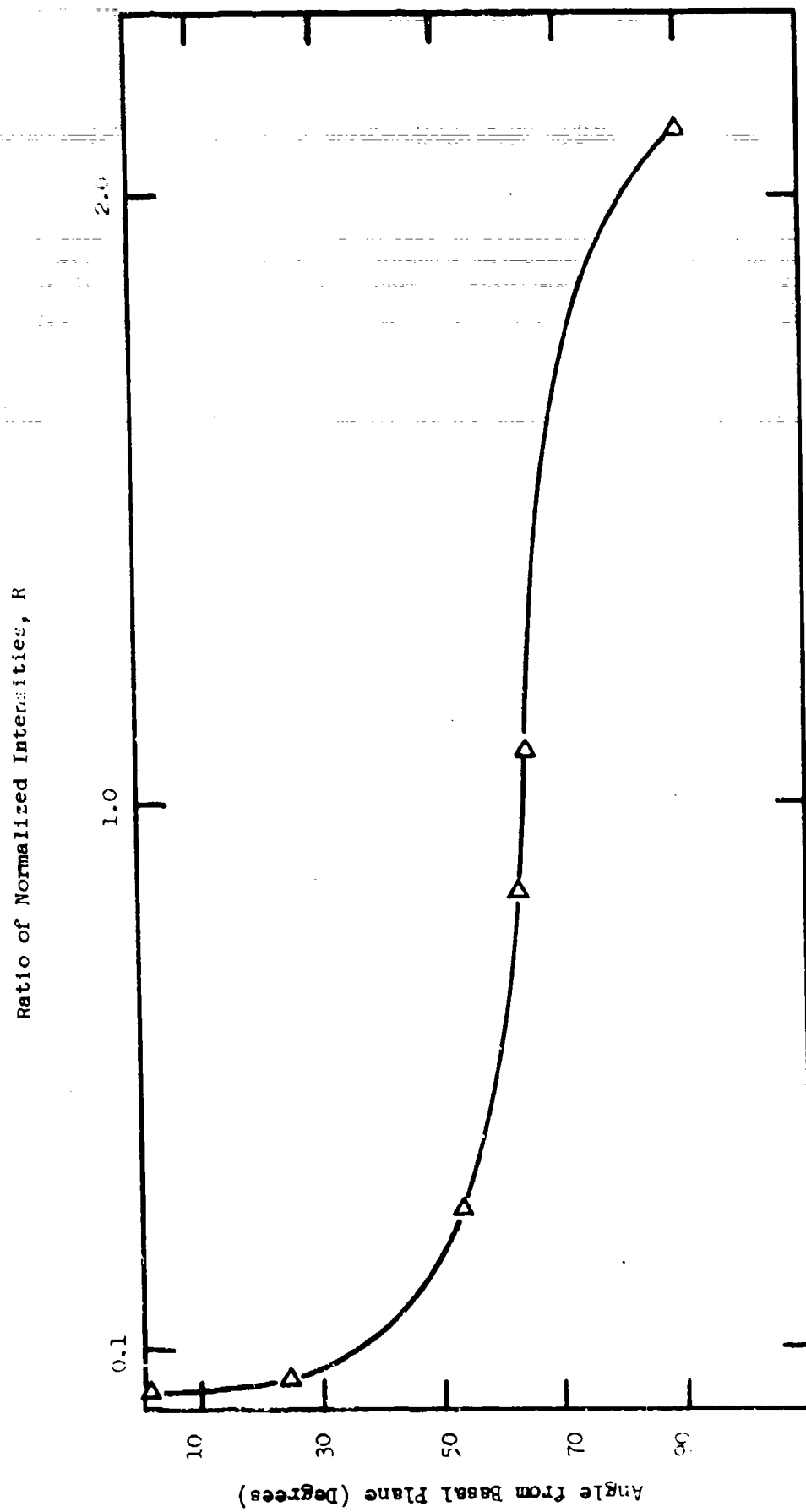


Figure 6. Inverse Pole Figure for Forged Silicon Nitride

TABLE IX  
Mechanical Properties of Forged  $Si_3N_4$

Billet	Bend Strength, ksi			Impact Strength*, in-lb <sup>0</sup>			
	23°C	1093°C	1316°C	23°C	1097°C	1200°C	1320°C
1905	113.9	61.9	46.0	2.94	7.03		3.75
	101.1	74.5	43.4				
	64.5	—	—				
	93.2	68.2	44.7				
1972	70.3	61.3	25.7	2.69	3.40	2.63	3.69
	60.3	65.3	41.5				
	83.1	69.3	30.5				
	71.2	65.3	32.6				

\*  $\frac{1}{2} \times \frac{1}{2}$  inch cross section.

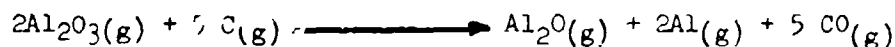
4. Problems of non-uniform distribution of residual porosity remains in forged  $\text{Si}_3\text{N}_4$ . Elimination of these large pores would undoubtedly be helpful in improving the strength of forged  $\text{Si}_3\text{N}_4$ .

#### IV. VOLATILE SPECIES IN HOT PRESSED $\text{Al}_2\text{O}_3$

##### A. General

Upon heat treatment, without pressure, hot pressed materials normally lose weight and density and in some cases the density loss may be quite high and accompanied by crack formation as well as pore coarsening. This has been attributed to expansion of gases trapped in pores and to the development of gases due to decomposition or reaction of chemical species in the annealing atmosphere. In some cases, residual molecules such as  $\text{OH}^-$ ,  $\text{SO}_4^{2-}$ ,  $\text{CO}_3^{2-}$  from incomplete powder calcining and subsequent powder handling are thought to be the source of the gaseous products. Experience has shown that such problems can result both from vacuum and ambient hot pressing. In addition to inhibiting final densification or causing subsequent bloating, these gaseous impurities can cause reduction of optical transparency, reduction of low temperature strength and reduction of high temperature strength and ductility. Consequently, this program has been concerned with understanding the gas/pore/property relationships in hot pressed  $\text{Al}_2\text{O}_3$ .

Recently<sup>2g</sup>, mass spectrographic studies of several hot pressed  $\text{Al}_2\text{O}_3$  bodies revealed that significant evolution of CO occurs on vacuum annealing. Further, in some cases, significant evolution of  $\text{Al}(\text{g})$  and  $\text{Al}_2\text{O}(\text{g})$  was observed at much lower temperatures than normally expected. This was interpreted as indicating the presence of free carbon in the hot pressed  $\text{Al}_2\text{O}_3$  resulting in reduction of the  $\text{Al}_2\text{O}_3$  by the reaction:



This conclusion was supported by the fact that chemical analysis has indicated carbon contents in hot pressed  $\text{Al}_2\text{O}_3$  to typically be in the range of 100-500 ppm.<sup>2d,20</sup> This is several orders of magnitude higher than can be attributed to CO entrapped in the pores from the hot pressing atmosphere. Therefore, significant additional carbon may be picked up from the hot pressing dies. There is no data on the solubility of C in  $\text{Al}_2\text{O}_3$  so it is not possible to know whether the carbon found is in the range expected for equilibrium solubility under the hot pressing conditions or whether it represents additional pickup from physical mixing, surface contamination on the powder, or gas transport and deposition of carbon during heating.

Therefore, it is of interest to measure the solubility of carbon in  $\text{Al}_2\text{O}_3$ . This must be done without formation of  $\text{Al}_4\text{C}_3$ ,  $\text{Al}_2\text{OC}$ , or  $\text{Al}_4\text{O}_4\text{C}$ . Therefore, to avoid direct contact with carbon which could lead to formation of these compounds<sup>21</sup>, the carbon content was determined after annealing in CO or  $\text{CO}_2$ ; the use of both gases was expected to further indicate whether there is a significant effect of the oxygen pressure on the carbon solubility; such an effect may be anticipated since the equilibrium defect

content is changed from metal deficient to oxygen deficient over the resultant range of  $P_{O_2}$ .

### B. Experimental

To minimize confusion from formation of carbides of impurity cations and to minimize diffusion times a high purity, submicron  $Al_2O_3$  powder was used.\* For all runs the powder was annealed for 16 hrs. at about  $1200^\circ C$  in a 0.25 atm of flowing  $CO_2$  prior to the actual anneal; this pretreatment should be sufficient to convert all of the residual  $\gamma$  powder to  $\alpha$ - $Al_2O_3$ , to remove residual gaseous impurities, and to burn out any initial carbonaceous impurities.

The annealings were done in a flowing atmosphere in a tube furnace. A double  $Al_2O_3$  tube furnace was used; the furnace was a Mo wound resistance furnace with  $H_2$  around the windings and between the two tubes. A sealed delivery and exit system was connected to the inner tube so that it could be evacuated prior to the runs. The gas delivery system allowed mixing of  $CO$ ,  $CO_2$ \*\*, and Ar to obtain the desired atmospheres; during the runs the pressure was maintained at 1 atm with a 10 cfph flow rate. The gases were passed over "Drierite" to remove excess water and the  $CO$  was passed over activated charcoal to remove any iron carbonyl. Heating was done under a mixture of 75% Ar and 25%  $CO_2$ . After the temperature was stabilized, the desired gas mixture was introduced and the samples were held for 4 hours. Annealings were done at  $1600^\circ$  and  $1700^\circ C$ ; these temperatures were selected after an initial run at  $1700^\circ C$  to obtain high enough carbon concentrations to allow satisfactory chemical analysis. Runs were made in pure  $CO$  or  $CO_2$  and in mixtures of 75% Ar - 25%  $CO$  and 75% Ar - 25%  $CO_2$  to determine the pressure dependence of the solubility. The runs with  $CO_2$  were cooled in the annealing mixture; for runs with  $CO$  the mixture was changed to Ar and  $CO_2$  below  $1200^\circ C$  to prevent contamination by  $CO$  decomposition. Cooling to below  $1200^\circ C$  took less than 2 hours.

For each run a batch of about 1 gram of powder was held in an  $Al_2O_3$  boat. The powder was not packed in order to minimize sintering during the runs and to maximize gas permeability. After the runs, the powder was slightly sintered but could easily be broken up. The chemical analysis was done by a standard fusion technique to measure the carbon content\*\*\*. Typically, the powder was divided in half and two determinations were made.

### C. Results

The carbon contents measured for each sample are reported in Table X. For several samples the variability between the two measurements was unexpectedly high; both values are given below the averages. For all cases the carbon contents were between 20 and 90 ppm. Determination of NBS

---

\*Batch B2335 Johnson-Matthey, Grade 2  $Al_2O_3$ . This is similar to the powder previously used for high purity  $Al_2O_3$  fabrication. Supplier reported purity for the previous lot was 99.9995%  $Al_2O_3$ ; however, spark source mass spectrographic analysis indicated about 40 ppm cation impurity.<sup>2d</sup>

\*\*The  $CO$  was 99.5% pure, the  $CO_2$  99.8% pure - suppliers reported purity.

\*\*\*The chemical analyses were done by M. L., Central Analytic Facility.

TABLE X

Apparent Carbon Solubility in  $Al_2O_3$

Temperature °C	Carbon Content, ppm (by weight)			
	$CO_2 - 1 \text{ atm}$	$CO_2 - \frac{1}{4} \text{ atm}$	$CO - 1 \text{ atm}$	$CO - \frac{1}{4} \text{ atm}$
1700	<sup>26</sup> (23/30)	<sup>60</sup> (32/88)	54	<sup>73</sup> (68/78)
1600	<sup>52</sup> (39/66)	<sup>74</sup> (69/80)	<sup>35</sup> (28/43)	

standards indicated reproducibility to be within a few ppm, so the differences are apparently significant. It can be seen that the solubility in CO may be slightly higher, but is not significantly different. In all cases, the apparent solubility was higher at 0.25 atm than at 1 atm of CO or CO<sub>2</sub>, which is opposite that expected. Further, the solubilities were apparently higher at 1600°C than 1700°C for the CO<sub>2</sub> which is also opposite that expected if a defect such as an interstitial or compensating vacancy must be formed in the Al<sub>2</sub>O<sub>3</sub> lattice.

The cause of the variability is not presently known. There is no data for diffusivity of C in Al<sub>2</sub>O<sub>3</sub> so it cannot be known for certain whether incomplete diffusion could be the cause. Since the variability was on a gross scale, it may indicate that the gas diffusion through the powder was limiting; if so, longer annealing times will be troubled by further sintering which will further reduce permeability to gas and result in particle coarsening which increases the solid diffusion distances. Several of the cation impurities, i.e., Si, Cr, Ti, and Fe could form carbides, particularly in CO; however, the total amount of these present would only account for a few ppm of C.

The inverse pressure dependence would suggest formation of Al<sub>2</sub>OC if free carbon were present. However, oxycarbide formation from the gases would have to go by one of the reactions:



or



The available thermodynamic data<sup>21</sup> indicates neither reaction should occur under any of the annealing conditions.

Although the solubility data are not entirely satisfactory, they do allow some inferences regarding the origin of carbon found in hot pressed Al<sub>2</sub>O<sub>3</sub>. During hot pressing the gas diffusion distances are larger and the times at temperature, before pore closure, are shorter than used here, so that pickup of carbon to levels in excess of 100 ppm indicates that carbon is present in excess of the solubility limit for CO. The value of 80 ppm C<sup>28</sup> measured in a vacuum hot pressed sample of similar high purity powder may be close to the equilibrium solubility expected for the particular hot pressing conditions. Additional work is required to resolve the uncertainties indicated here and to allow inference as to the state of CO or CO<sub>2</sub> dissolved in Al<sub>2</sub>O<sub>3</sub>.

#### D. Conclusions

1. Carbon contents of Al<sub>2</sub>O<sub>3</sub> powder annealed at 1600° - 1700°C in CO and CO<sub>2</sub> were in the range of 26-74 ppm by weight. The variability within samples indicates these may only be approximate indications of the actual solubility of C for these conditions.



2. This carbon content is below that typically measured in not pressed  $Al_2O_3$  billets and so is compatible with the view that after hot pressing there is significant carbon present beyond that associated with gas solubility.

#### V. REFERENCES

1. C.D. Pears and H. Starrett, "An Experimental Study of the Weibull Volume Theory," AFML-TR-66-228.
2. a. A.H. Heuer, W.H. Rhodes, D.J. Sellers, and T. Vasilos, "Microstructure Studies of Polycrystalline Refractory Oxides," NOW-66-0506(d), Summary Report (1967).  
b. W.H. Rhodes, D.J. Sellers, R.M. Cannon, A.H. Heuer, W.R. Mitchell, and P.L. Burnett, "Microstructure Studies of Polycrystalline Refractory Oxides," Contract N00019-67-C-0336, Summary (1968).  
c. W.H. Rhodes, P.F. Jahn, P.L. Burnett, "Microstructure Studies of Refractory Polycrystalline Oxides," Contract N00019-68-C-0108 (June 1969).  
d. W.H. Rhodes and R.M. Cannon, "Microstructure Studies of Refractory Polycrystalline Oxides," Contract N00019-69-C-0198, (December 1969).  
e. W.H. Rhodes and R.M. Cannon, "Microstructure Studies of Refractory Polycrystalline Oxides," Contract N00019-70-C-0171.  
f. W.H. Rhodes, P.L. Berneburg, and R.M. Cannon, "Microstructure Studies of Refractory Polycrystalline Oxides," Contract N00019-71-C-0325 (January 1972).  
g. W.H. Rhodes, P.L. Berneburg, R.M. Cannon, W.C. Steele, "Microstructure Studies of Polycrystalline Refractory Oxides," N00019-72-0298 (April 1973).
3. D.L. Vrooman and J.E. Ritter, Am. Ceram. Soc. Bull. 49, 789 (1970).
4. E.B. Shad, J. Am. Ceram. Soc., 48, 43 (1965).
5. H.P. Kirchner, R.M. Gruver, R.E. Walker, J. Am. Ceram. Soc., 56 17 (1973).
6. R.J. Charles and R.R. Shaw, "Delayed Failure of Polycrystalline and Single Crystal Alumina," General Electric Report No. 62-RL-3081M.
7. E.M. Passmore, R.M. Spriggs, and T. Vasilos, J. Am. Ceram. Soc., 48, 1 (1965).
8. R.M. Spriggs, J.B. Mitchell, and T. Vasilos, J. Am. Ceram. Soc., 47, 323 (1964).

9. R.W. Rice, Proc. Brit. Ceram. Soc., 20, 205 (1972).
10. a. Carniglia, S.C., J. Am. Ceram. Soc., 48, 580 (1965).  
b. Carniglia, S.C., Am. Ceram. Soc. Bull., 50, 184 (1971).
11. S. Weiderhorn, J. Am. Ceram. Soc., 52, 485 (1969).
12. G.D. Swanson, J. Am. Ceram. Soc., 55, 48 (1972).
13. P.L. Gutshall and G.E. Gross, Eng. Fract. Mech. 1, 463 (1969).
14. L.A. Simpson, J. Am. Ceram. Soc., 56, 7 (1973).
15. R.L. Coble, J. Am. Ceram. Soc., 45, 123 (1962).
16. S.K. Roy and R.L. Coble, J. Am. Ceram. Soc., 50, 435 (1967).
17. A.H. Heuer, D.J. Sellers, and W.H. Rhodes, J. Am. Ceram. Soc., 50, 468 (1967).
18. W.H. Rhodes and R.M. Cannon, Jr., "High Temperature Compounds for Turbine Vanes," NASA CR-134531 (January 1974).
19. D.R. Platts, H.P. Kirchner and R.M. Cruver, "Strengthening of Oxidation Resistant Materials for Gas Turbine Applications," NASA CR-121002.
20. D. Sellers and J.E. Niesse, "The Development of Hot Pressed Alumina for Gas Bearing Applications," Final Report, Contract N00030-66-C-0189 (28 February 1969).
21. J.H. Cox and L.M. Pidgeon, Can. J. of Chem., 41, 671 (1963).